EXPERIMENTAL STUDY FOR THE PRODUCTION CROSS SECTION OF β^+ EMITTERS FOR RANGE VERIFICATION IN PROTONTHERAPY

MASTER THESIS, DECEMBER 2017

INTER-UNIVERSITARY MASTER'S DEGREE IN NUCLEAR PHYSICS

UNIVERSIDAD Ð SEVILLA

Author:

María Teresa Rodríguez González

Supervised by:

Dr. Carlos Guerrero Sánchez
Dr. Mª del Carmen Jiménez Ramos

Acknowledgements

I would like to express my sincere gratitude to my supervisors Dr. Carlos Guerrero and Dr. María del Carmen Jiménez, for the continuous support in the realization of this work, for their patience, encouragement, all the good advices and guidances with which I have improved my knowledges and skills in experimental physics. I always could count on their help, and their enthusiasm and motivation has made me to be pleased doing this research work.

In addition, I would like to express my thankfulness to the personnel at CNA and Physics Faculty who has contributed to the manufacturing of the material and the realization of the experiments, for their assistance and collaboration. Specially, I would like to thank Ángel Parrado, for his immediate availability and compromise with the PET/CT analysis.

Abstract

In protontherapy, the uncertainties in the range of the beam delivered to the patient result in some safety margins in the planning that limit the dose that can be delivered to the tumour. For this reason, there is an intensive research program aiming at *in vivo* range verification.

In particular, positron emitters are induced on C, N, O, Ca and P nuclei by the protons of the beam in the patient. Based on this, *in vivo* PET range verification relies on the comparison of measured and simulated activity distributions of these isotopes. The accuracy of the simulated distribution depends on the accuracy of the cross section for the production of these positron emitters. A revision of the experimental data available in the EXFOR database shows that the corresponding cross sections do not always cover the full energy range of interest, and that there are sizeable differences between the different measurements.

The aim of this study is to develop a method for measuring the production cross sections of the positron emitters ^{11}C and ^{13}N in the most abundant isotopes in human body: C, N and O. This will be used, in a first step, to measure the cross section of positron emitters produced by a low energy proton beam at the CNA cyclotron. The 18 MeV energy beam produced by the cyclotron is degraded using a multi-stack target configuration in order to obtain the cross section in different energy points. The activity induced by the beam has been measured using a clinical PET scanner. The production cross section of these reaction channels have been measured and compared with the available data, showing a reasonable agreement with them within uncertainties.

Contents

Abstract **IV**

List of Figures **VII**

List of Tables **X**

1 Introduction **1**
1.1 A brief history of protontherapy 1
1.2 Proton interaction mechanisms 2
1.3 Range of protons in human body 4
1.4 Range verification in protontherapy with PET 5
1.5 Production yields of β^+ isotopes for range verification 8
1.6 Objectives 13

2 Experimental set-up: description and characterization **14**
2.1 18 MeV proton cyclotron at CNA 14
2.2 PET/CT scanner at CNA 16
2.3 Target configuration for irradiation 21

3 Experiments at CNA, analysis and results **25**
3.1 Irradiation and PET measurement 25
3.2 Fitting activity curves 27
3.3 Production yields and cross sections 34
3.4 Comparison to previous data 40

4 Conclusion and outlook **45**

Bibliography **47**

List of Figures

1.1 *The spread out Bragg peak (SOBP, dashed blue line) is the therapeutic radiation distribution. The SOBP is the sum of several individual Bragg peaks (thin blue lines) at different depths. The depth-dose plot of an X-ray beam (red line) is provided for comparison. [9]* 2

1.2 *Right: Mass stopping power (S) versus energy (E) for protons in liquid water. The corresponding range (R), calculated using the plotted S values and on the assumption of the continuous slowing down approximation (CSDA), is also plotted [1]. Left: Range of protons in water [13].* 5

1.3 *Dashed line and right axis: Bragg curve (the dose deposited as a function of depth for a 160 MeV proton beam). Left axis: total (dotted line) and primary (solid line) proton fluence as a function of depth, showing the contributions from secondary protons generated in nuclear interactions. The decrease in the entrance plateau is due to primary protons undergoing nuclear interactions whereas the sharp decrease at the Bragg peak is mainly due to the stopping of primary protons. The lower graph shows the dose profile, illustrating the enlargement of the beam due to multiple Coulomb scattering. [12]* 6

1.4 *Safety margins applied at different clinical protontherapy facilities: Loma Linda University Medical Center (LLUMC), Universität Protonen Therapie Dresden (UPTD), Massachusetts General Hospital (MGH) and University of Florida Health Proton Therapy institute (UFH). Range bonus refers to the margin added to the prescribed range to ensure full tumour coverage even in the case of an undershoot [16].* 7

1.5 *Available data for the production cross sections of the reaction channel* $^{12}C(p,*)^{11}C$ *and* $^{13}C(p,*)^{11}C$*, in a range from 0 to 1 GeV. The data is provided by EXFOR.* 10

1.6 *Available data for the production cross sections of the reaction channel* $^{12}C(p,*)^{13}N$ *and* $^{13}C(p,*)^{13}N$*, in a range from 0 to 30 MeV. The data is provided by EXFOR.* 10

1.7 *Available data for the production cross sections of the reaction channel $^{16}O(p,*)^{11}C$, in a range from 0 to 160 MeV. The data is provided by EXFOR.* 11
1.8 *Available data for the production cross sections of the reaction channel $^{16}O(p,*)^{13}N$, in a range from 0 to 160 MeV. The data is provided by EXFOR.* 11
1.9 *Available data for the production cross sections of the reaction channel $^{14}N(p,\alpha)^{11}C$, in a range from 0 to 30 MeV. The data is provided by EXFOR.* 12
1.10 *Available data for the production cross sections of the reaction channel $^{14}N(p,*)^{13}N$, in a range from 0 to 160 MeV. The data is provided by EXFOR.* 12

2.1 *Scheme of the cyclotron external line.* 15
2.2 *Left: 18 MeV (protons)/9 MeV (deuterons) cyclotron accelerator. Right: Experimental set-up, where one can see the sample holders with the different targets inside them, the external beam and the monitored table.* 15
2.3 *Left: PMMA irradiated targets, which are scanned with a Epson Perfection V700 Photo Scanner. Right: Irradiation intensity of the PMMA-9 target.* . 16
2.4 *Horizontal (left) and vertical (right) profile of the irradiation colouration in PMMA-9 target, for three different vertical positions. PMMA films are not radiochromic films and thus they can not measure the dose deposition profile, although they allow to measure the beam size.* 16
2.5 *PET/CT Scanner at the CNA facilities.* 17
2.6 *Left: Template of the polyethylene sheet built for the emplacement of the ^{22}Na source. Right: PET/CT scanning system and set up of the polyethylene sheets covering the sample.* 19
2.7 *Spatial calibration in efficiency for each position.* 20
2.8 *3D representation of the PET scanner efficiency, for plane y=1 (left) and plane y=2 (right).* 21
2.9 *Example of the entering and exiting proton beam in PE-2 target.* 23
2.10 *Energy distribution after the proton beam traverse each target. The blue line is the number of protons in each energy interval and the red line is the gaussian fitting curve.* 24

3.1 *Current beam measured in a graphite, for each irradiation, as well as the total charge.* 26
3.2 *Polyethylene matrix with irradiated targets inside the PET scanner.* 27
3.3 *PET images superposed to CT image in the three planes, for y=1 and y=2.* 27
3.4 *Activity curve in function of time in the first PE film of each set of targets.* 29

3.5 *Fitted activity curve in PMMA targets. The blue line represents the fitted activity of ^{13}N, the green line represents the activity curve of ^{11}C and the red line the total fit, including background.* 30
3.6 *Fitted activity curve in PE targets. The blue line represents the fitted activity of ^{13}N, the green line represents the activity curve of ^{11}C and the red line the total fit, including background.* 31
3.7 *Fitted activity curve in Nylon-6 targets. The blue line represents the fitted activity of ^{13}N, the green line represents the activity curve of ^{11}C and the red line the total fit, including background.* 32
3.8 *Production cross section for nuclear reactions of interest.* 37
3.9 *Production cross section of positron emitter ^{11}C measured in ^{nat}C and the experimental data available in EXFOR.* 42
3.10 *Production cross section of positron emitter ^{13}N measured in ^{nat}C and the experimental data available in EXFOR.* 42
3.11 *Production cross section of positron emitter ^{11}C measured in ^{nat}O and the experimental data available in EXFOR. The threshold is out of the energy range.* 43
3.12 *Production cross section of positron emitter ^{13}N measured in ^{nat}O and the experimental data available in EXFOR.* 43
3.13 *Production cross section of positron emitter ^{11}C measured in ^{nat}N and the experimental data available in EXFOR.* 44
3.14 *Production cross section of positron emitter ^{13}N measured in ^{nat}N and the experimental data available in EXFOR.* 44

List of Tables

1.1 Summary of proton interaction types, targets, ejectiles, influence on projectile and selected dosimetric manifestations. [1] 3
1.2 Target nuclei, positron emitters, and reaction channels of interest for the cross section measurements. [1] [17] 8

2.1 PROPCPS of the different β^+ sources, measured in several positions during ten minutes. 18
2.2 PROPCPS of the different β^+ sources, measured in a fixed positions during two and ten minutes. The conversor is polyethylene. 18
2.3 Target configuration for the irradiation. The uncertainty in the thickness was estimated of the standard deviation of three independent measurements. The geometry of the films is square (40×40 mm^2). 22

3.1 Experimental configuration during irradiation and PET/CT detection. . . 26
3.2 Correction factor by decay during the irradiation. 28
3.3 Initial activity in each target of PE. (*) The results of these fit are too small and can not be trusted data, due to the low production yield of 11C in PE targets. 33
3.4 Initial activity in each target of PMMA. 33
3.5 Initial activity in each target of Nylon. 34
3.6 Targets composition. 35
3.7 Production cross section measurement in C_{nat}. (*) The results of these fit are too small and can not be trusted data, due to the low production yield of 11C in PE targets. Then the cross sections are compatible with zero. . . 38
3.8 Production cross section measurement in ^{16}O. (*) The results of these fit are too small and can not be trusted data, due to the low production yield in comparison with the contribution of C producing ^{11}C and ^{13}N. 39
3.9 Production cross section measurement in ^{14}N. 40

1. Introduction

1.1 A brief history of protontherapy

The physics of protontherapy has advanced considerably since, in 1946, Robert Wilson proposed to use accelerator-produced beams of protons to treat tumours in humans [1, 2]. The principal reason to use protontherapy over radiotherapy is its superior spatial dose distribution in the patient (see figure 1.1). In comparison to photon therapy, proton beam therapy results in a lower radiation dose to the adjacent normal tissue due to the characteristics of proton beams: a well-defined, finite penetration depth in matter and a high dose deposition close to the end of the trajectory, the Bragg Peak. In order to achieve an homogeneous dose over the entire tumour, protons of different energies, i.e. with Bragg peaks at different depths, are applied. The sum of all the Bragg peaks, shown in figure 1.1, is called the spread-out Bragg peak (SOBP).

In 1954, the first human was treated with proton beams at the Lawrence Berkeley Laboratory [3]. In 1962, specialized radiosurgical proton treatments commenced at the Harvard Cyclotron Laboratory [4, 5], followed in the mid 1970s by treatments for ocular cancers [6] and larger tumours [7]. Physicists at Harvard, collaborating with clinical colleagues at the Massachusetts General Hospital, the Massachusetts Eye and Ear Infirmary, and elsewhere, developed much of the physics and technology needed to treat patients with proton beams safely and effectively. Remarkably, the research and development program at Harvard continued for more than 40 years. During the same period, physicists were developing other key related technologies, such as accelerators, magnetically scanned beams, treatment planning systems, computed tomography imaging (CT) and magnetic resonance imaging [1].

However, the widespread use of proton therapy has been slow in comparison to other techniques, for instance intensity-modulated photon therapy. There are several reasons for this, including technical difficulty, high cost and lack of evidence of cost-competitiveness. Although commercial proton delivery systems appeared in 2001, the cost of proton therapy

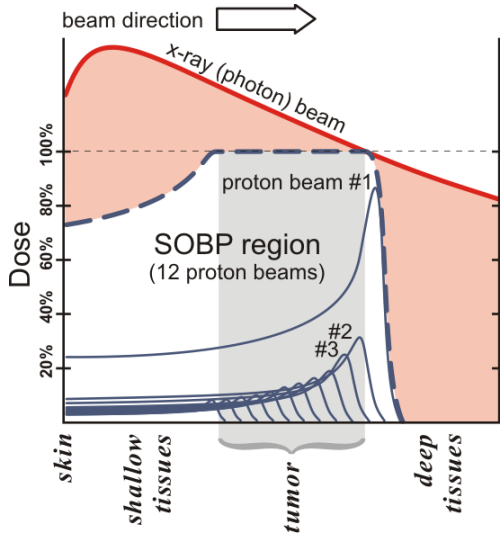

Figure 1.1: *The spread out Bragg peak (SOBP, dashed blue line) is the therapeutic radiation distribution. The SOBP is the sum of several individual Bragg peaks (thin blue lines) at different depths. The depth-dose plot of an X-ray beam (red line) is provided for comparison. [9]*

equipment remains significantly higher than that of comparable photon therapy equipment [1]. But prices are being continuously reduced and clinical evidence of the advantages of protontherapy are being demonstrated. Hence, today there are 64 protontherapy centres in operation worldwide, with 15 more under construction. Overall, the Particle Therapy Cooperative Group (PTCOG) estimates that at least 131240 patients had been treated between 1954 and 2015 [8].

1.2 Proton interaction mechanisms

Protontherapy uses a precision-focused proton beam to target and treat tumours. On their way through matter, protons interact with the nuclei and electrons that they encounter. The predominant types of interactions are Coulombic interactions with atomic electrons, Coulombic interactions with the atomic nucleus, nuclear reactions and Bremsstrahlung. Table 1.1 summarizes the proton interaction types, targets, principal ejectiles, influence on the proton beam and the dosimetric manifestation. In a first order approximation, protons continuously lose kinetic energy via frequent inelastic Coulombic interactions with

Interaction type	Interaction target	Principal ejectiles	Influence on projectile	Dosimetric manifestation
Inelastic Coulomb scattering	Atomic electrons	Primary proton, ionization electrons	Quasi-continuous energy loss	Energy loss determines range in patient
Elastic Coulomb scattering	Atomic nucleus	Primary proton, recoil nucleus	Change in trajectory	Determines lateral penumbral sharpness
Non elastic nuclear reactions	Atomic nucleus	Secondary protons and heavier ions, neutrons and gamma rays	Removal of primary proton from beam	Primary fluence, generation of stray neutrons, generation of prompt gammas for *in vivo* interrogation
Bremsstrahlung	Atomic nucleus	Primary proton, Bremsstrahlung photon	Energy loss, change in trajectory	Negligible

Table 1.1: Summary of proton interaction types, targets, ejectiles, influence on projectile and selected dosimetric manifestations. [1]

atomic electrons. Most protons travel in a nearly straight line because their rest mass is ∼2000 times greater than that of an electron. When a proton undergoes a nuclear reaction it disappears, producing secondary radiation (light particles and photons) and producing a new nucleus. On the other hand, when the proton undergoes elastic scattering with a nucleus, its trajectory can be affected significantly, thus creating the so-called penumbra of the beam.

As mentioned above, fast charged particles moving through matter interact with the electrons of atoms via inelastic Coulomb scattering. The interaction excites or ionizes the atoms, leading to an energy loss of the travelling particle. In this context, it is convenient

to define the mass stopping power, which express the energy loss rate in a way that is independent of the mass density, as

$$\frac{S}{\rho} = -\frac{dE}{\rho dx}, \tag{1.1}$$

where ρ is the mass density of the absorbing material, E is the mean energy loss and x is the distance. The energy loss rate was described by Bethe [10] and Bloch [11], taking into account quantum mechanical effects, and is given by

$$\frac{S}{\rho} = 4\pi N_A r_e^2 m_e c^2 \frac{Z}{A}\frac{z^2}{\beta^2}\left[ln\frac{2m_e c^2\gamma^2\beta^2}{I} - \beta^2 - \frac{\delta}{2} - \frac{C}{Z}\right], \tag{1.2}$$

where N_A is Avogadro's number, r_e is the classical electron radius, m_e is the mass of an electron, z is the charge of projectile, Z is the atomic number of the absorbing material, A is the atomic weight of the absorbing material, c is speed of light, $\beta = v/c$, where v is the velocity of the projectile, $\gamma = (1-\beta^2)^{-1/2}$, I is the mean excitation potential of the absorbing material, δ is the density corrections arising from the shielding of remote electrons by close electrons and will result in a reduction of energy loss at higher energies, and C is the shell correction item, which is important only for low energies where the particle velocity is near the velocity of the atomic electrons. Figure 1.2 (right) shows the dependence of the mass stopping power with the proton energy, illustrating how in the limit $\beta << 1$, the energy loss rate is proportional to v^{-2}, and thus near the end of the proton trajectory, at low velocity, the energy loss is higher, hence causing the Bragg peak.

1.3 Range of protons in human body

The range is defined as the depth at which half of protons in the medium have come to rest. There are small variations in the energy loss of individual protons (resulting in the range straggling), so the range is inherently an average quantity defined for a beam and not for individual particles. As the path of most protons in matter is nearly a straight line, the proton's pathlength is nearly equal to its projected pathlength and range. This fact allows for the proton range calculation with relatively simple numerical or analytical approaches [1].

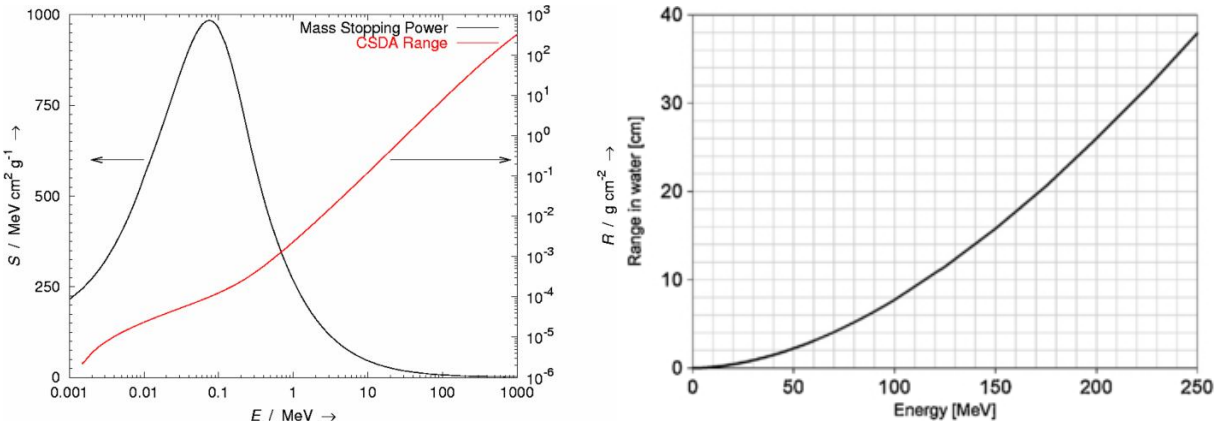

Figure 1.2: *Right: Mass stopping power (S) versus energy (E) for protons in liquid water. The corresponding range (R), calculated using the plotted S values and on the assumption of the continuous slowing down approximation (CSDA), is also plotted [1]. Left: Range of protons in water [13].*

As it is shown in figure 1.2 (left), in order to irradiate superficial tumours (few cm depth) a proton beam of 60-70 MeV is enough, whereas for deep (∼30 cm depth) tumour tissues is needed a higher proton beam energy (230-250 MeV). Consequently, clinical treatments use accelerators that typically produce protons with energies in the range of 70 to 250 MeV. During the irradiations, it is necessary to control where the protons deposit their energy, in order to reduce damage in normal tissues, and so that SOBP region corresponds with the tumour. For this reason, the proton beam range must be well calculated and, if possible, monitored.

In figure 1.3 we can see an example of protons range and Bragg peak, for a protons beam of 160 MeV in water. This figure shows how the maximum dose deposited in tissues (Bragg peak) corresponds with the last few centimetres of the range, being this one of the advantages in the use of proton therapy over photon therapy.

1.4 Range verification in protontherapy with PET

In current treatment plannings, a safety margin from 1% to 3% is usually applied (see figure 1.4). This means nearly 1 cm in a 30 cm deep tumour, which certainly limits the benefits of having a sharp Bragg peak. Reducing this uncertainty would allow a better utilization of the advantages of protontherapy over radiotherapy.

In a protontherapy treatment, one can detect the particles resulting from the nuclear

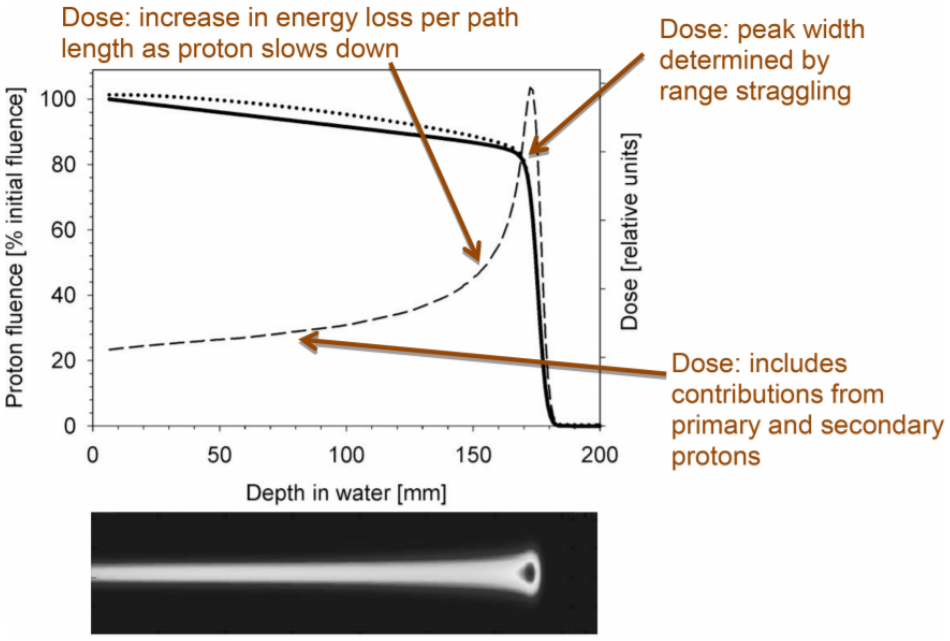

Figure 1.3: *Dashed line and right axis: Bragg curve (the dose deposited as a function of depth for a 160 MeV proton beam). Left axis: total (dotted line) and primary (solid line) proton fluence as a function of depth, showing the contributions from secondary protons generated in nuclear interactions. The decrease in the entrance plateau is due to primary protons undergoing nuclear interactions whereas the sharp decrease at the Bragg peak is mainly due to the stopping of primary protons. The lower graph shows the dose profile, illustrating the enlargement of the beam due to multiple Coulomb scattering. [12]*

interactions that protons suffer on their way trough the matter in order to monitor the beam range. These particles can be photons, neutrons or charged particles. In the case of photons, there are two kinds: prompt γ-rays and delayed γ-rays. Prompt γ-rays are emitted in the decay of excited atomic nuclei, in a nanosecond scale, hence during the irradiation. On the other hand, delayed γ-rays are the result of the decay of the unstable nuclei produced in nuclear reactions. When this decay is in the terms of β^+, two γ-rays of 511 keV are emitted in opposite directions. These simultaneous γ-rays can be detected in coincidence by a clinical Positron Emission Tomography (PET), and thus serve to determinate the range of the proton beam *in vivo*, shortly after the irradiation. [14]

Therefore, verification of the treatment and, in particular, of the beam range in the patient can be achieved by comparing the measured β^+ activity with predictions based on the treatment plan, the patient anatomy and the time course of irradiation and imaging.

There are three operational modalities for PET verification of proton therapy, based on

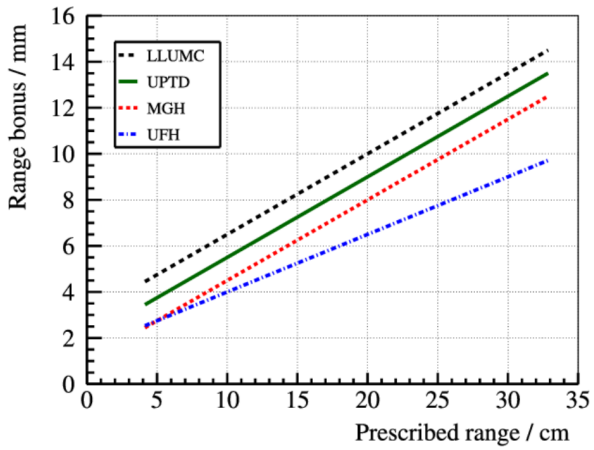

Figure 1.4: *Safety margins applied at different clinical protontherapy facilities: Loma Linda University Medical Center (LLUMC), Universität Protonen Therapie Dresden (UPTD), Massachusetts General Hospital (MGH) and University of Florida Health Proton Therapy institute (UFH). Range bonus refers to the margin added to the prescribed range to ensure full tumour coverage even in the case of an undershoot [16].*

the PET system used for data acquisition. In-beam PET uses detectors panels attached to the proton treatment system so that the data can be acquired during and immediately after treatment. In-room PET uses a independent PET scanner positioned within the treatment room to scan the patient (still in the treatment bed) soon after treatment. Off-line PET uses an established PET scanner close to but outside the treatment site, often with a CT component. [15]

The elements in the human body relevant for the production of positron emitters are mainly carbon, nitrogen, oxygen, phosphorus and calcium. The most copiously produced short-life (seconds) positron emitters are ^{12}N on carbon, ^{29}P on phosphorus, and ^{38m}K on calcium, and the most long-lived (minutes) positron emitters are ^{11}C, ^{13}N and ^{15}O [14].

As PET range verification relies on the comparison of measured and simulated activity distributions, the accuracy of the simulated distribution depends on the accuracy of the Monte Carlo codes, and thus, as Parodi et al. affirms in *"Experimental study on the feasibility of in-beam PET for accurate monitoring of proton therapy"* [19], this accuracy depends on the underlying cross section data.

Target	Abundance	Reaction channel	Half-life (min)	Threshold (MeV)
12C	98.9%	^{12}C(p,p+n)^{11}C	20.39	17.88
		^{12}C(p,γ)^{13}N	9.965	0
^{13}C	1.1%	^{13}C(p,t)^{11}C	20.39	16.36
		^{13}C(p,n)^{13}N	9.965	3.24
^{14}N	99.6%	^{14}N(p,α)^{11}C	20.39	3,13
		^{14}N(p,p+n)^{13}N	9.965	8.93
^{16}O	99.8%	^{16}O(p,3n+3p)^{11}C	20.39	57.59
		^{16}O(p,p+n+α)^{11}C	20.39	27.51
		^{16}O(p,p+d+t)^{11}C	20.39	46.21
		^{16}O(p,d+α)^{11}C	20.39	25.15
		^{16}O(p,2p+2n)^{13}N	9.965	35.63
		^{16}O(p,2d)^{13}N	9.965	29.10
		^{16}O(p,p+t)^{13}N	9.965	26.61
		^{16}O(p,α)^{13}N	9.965	5.55

Table 1.2: Target nuclei, positron emitters, and reaction channels of interest for the cross section measurements. [1] [17]

1.5 Production yields of β^+ isotopes for range verification

The three most abundant elements in the human body are oxygen (65%), carbon (18%) and nitrogen (3%). The interaction of a proton beam with these nuclei produces mainly the positron emitters ^{11}C (20.39 min) and ^{13}N (9.965 min) via the nuclear reactions listed in table 1.2. The experimental data available in EXFOR for those cross sections are displayed in figures 1.5−1.10.

The situation can be summarized as follow:

- In the case of the nuclear reaction ^{nat}C(p,*)^{11}C, the range of interest is covered all the way up to 250 MeV. There are large discrepancies near the threshold below 20 MeV and moderate (∼10%) differences between data sets in the range.

- The reaction ^{nat}C(p,*)^{13}N has only been studied below 30 MeV, and mostly looking at reactions on ^{13}C. The agreement between the data available is in the order of 20%.

- The production cross section of the nuclear reaction ^{nat}O(p,*)^{11}C is not well known.

At high protontherapy energies there is not any available data, and at low energies there is not a good agreement between the only two measurements available.

- In the case of ^{nat}O(p,*)^{13}N, there are a good number of measurements in agreement in a range of energies until 20 MeV. In the tens at MeV region, the few available data differ considerably with each other, and they cover only up to 140 MeV.

- The reaction channel ^{nat}N(p,*)^{11}C has been abundantly measured at low energies (below 30 MeV), although one set of data is not in a good agreement with the rest (30% difference). However, at the higher energies of interest in protontherapy there are only two data points.

- The production cross section of the nuclear reaction ^{nat}N(p,*)^{13}N is not well known either. EXFOR contains only a few set of data at low energies (up to 30 MeV), and the differences between them are around the 20%.

On the other hand, there are some reactions that can not be studied easily, because the target isotopes have a small abundance, so their contribution to the total cross section is negligible. This is the case of ^{15}N(p,2p3n)^{11}C, ^{15}N(p,p2n) ^{13}N and those reactions derived from the least abundant isotopes of oxygen.

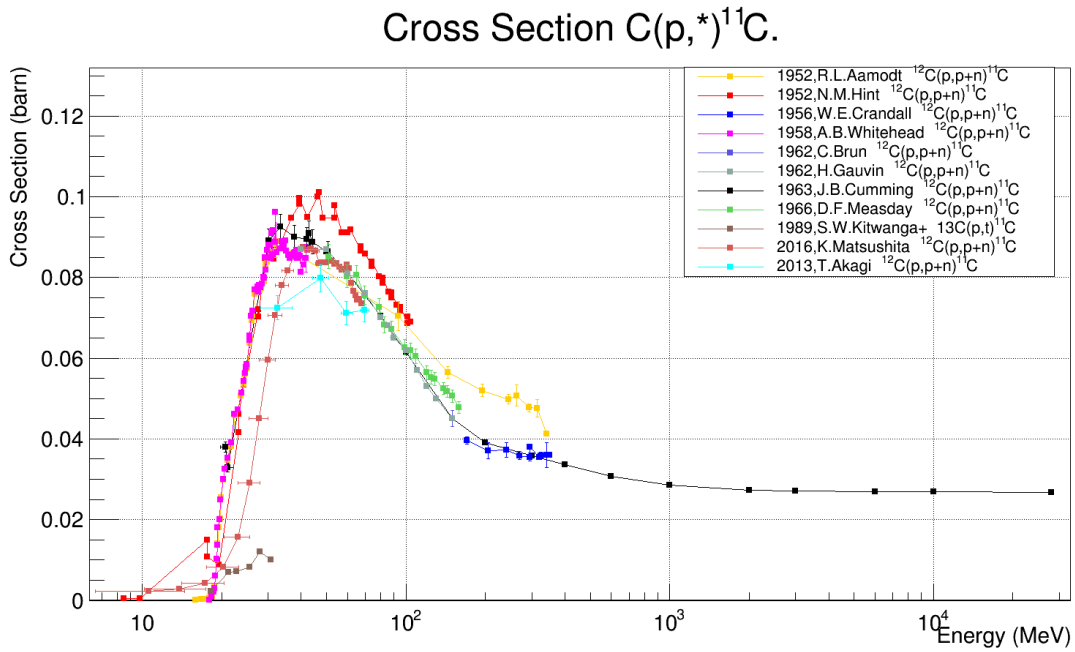

Figure 1.5: *Available data for the production cross sections of the reaction channel* $^{12}C(p,*)^{11}C$ *and* $^{13}C(p,*)^{11}C$*, in a range from 0 to 1 GeV. The data is provided by EXFOR.*

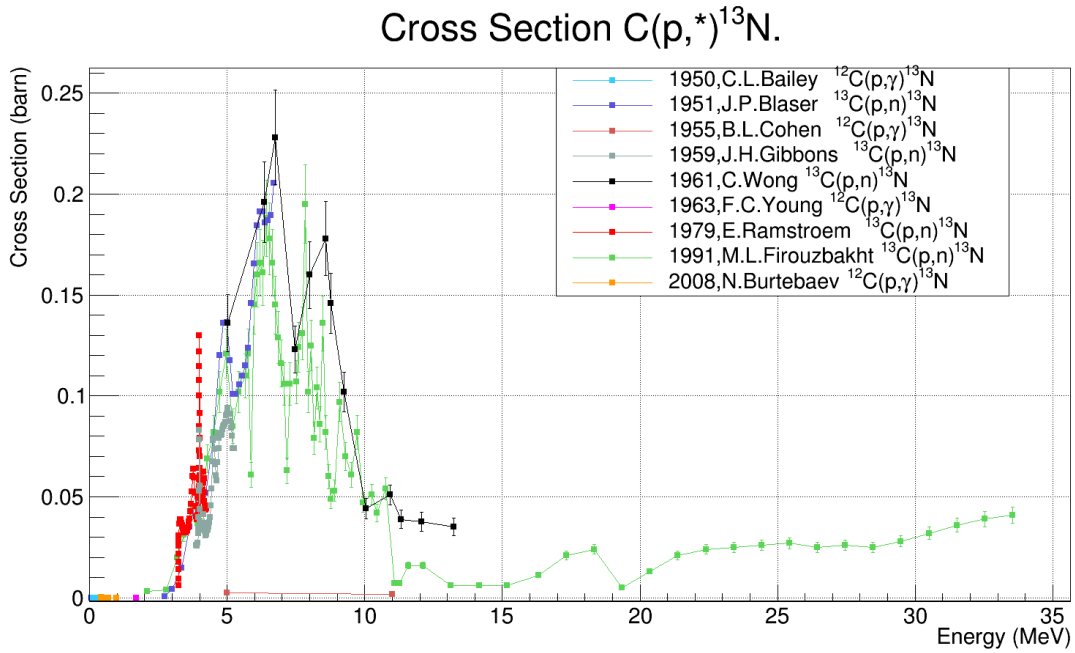

Figure 1.6: *Available data for the production cross sections of the reaction channel* $^{12}C(p,*)^{13}N$ *and* $^{13}C(p,*)^{13}N$*, in a range from 0 to 30 MeV. The data is provided by EXFOR.*

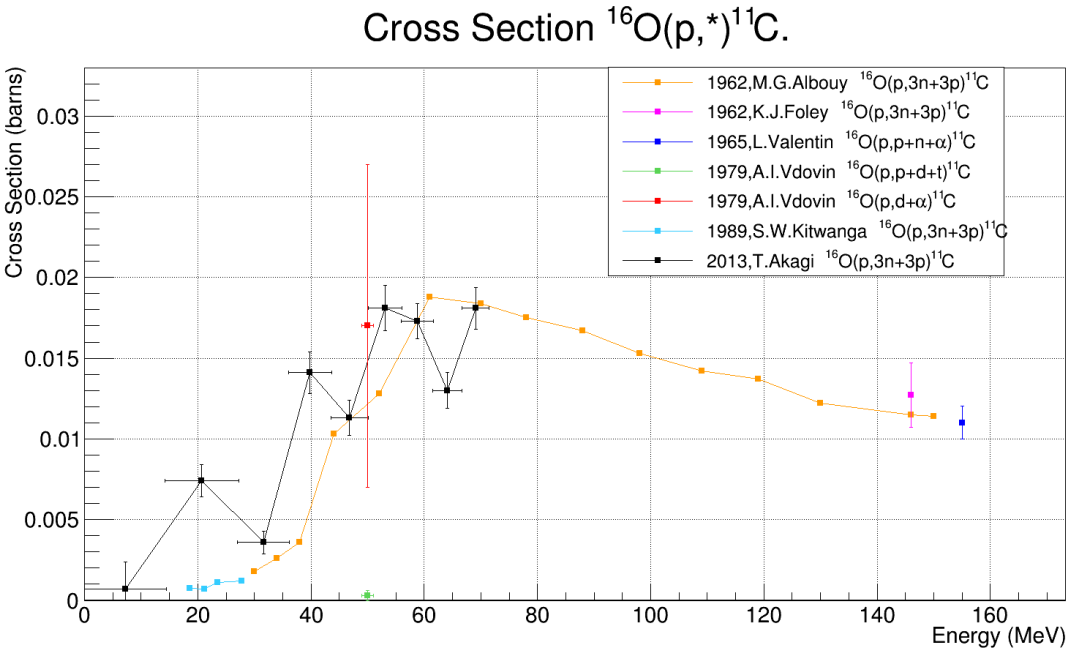

Figure 1.7: *Available data for the production cross sections of the reaction channel* $^{16}O(p,*)^{11}C$*, in a range from 0 to 160 MeV. The data is provided by EXFOR.*

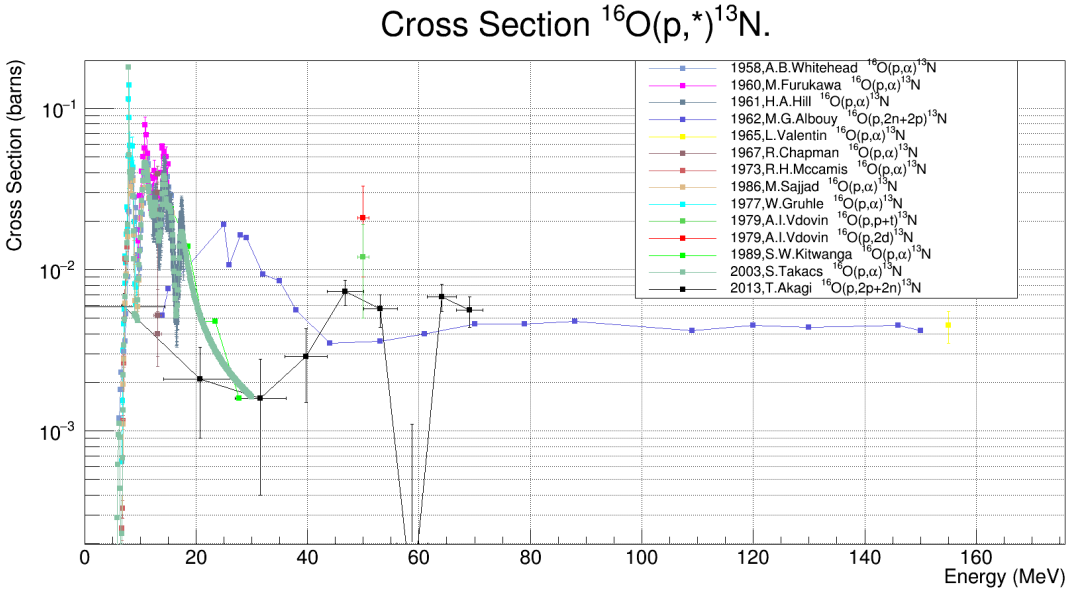

Figure 1.8: *Available data for the production cross sections of the reaction channel* $^{16}O(p,*)^{13}N$*, in a range from 0 to 160 MeV. The data is provided by EXFOR.*

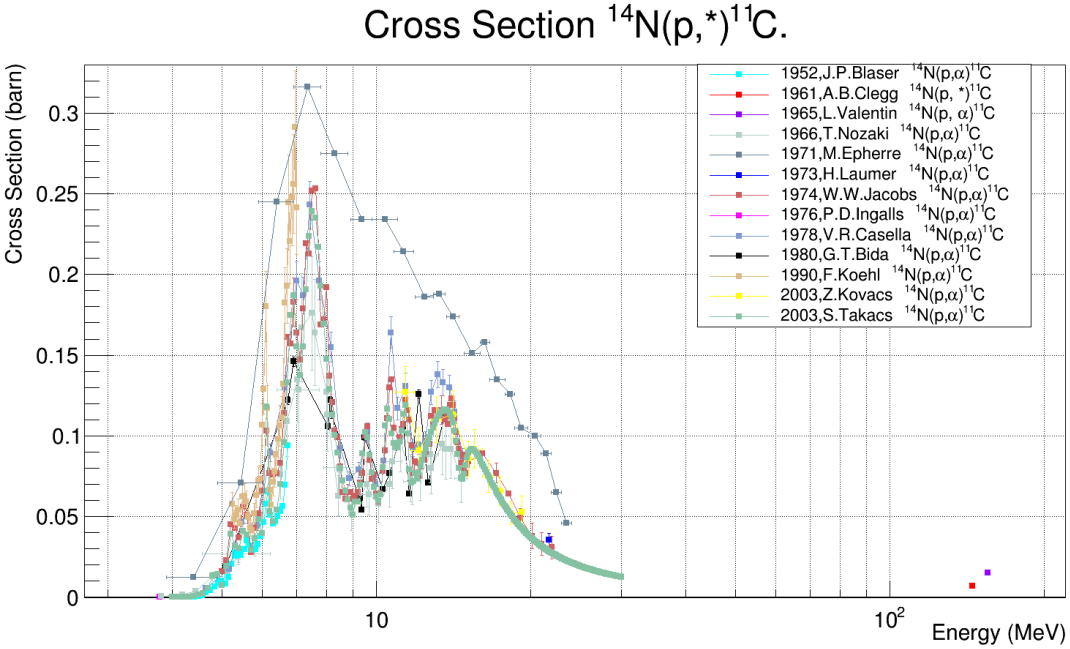

Figure 1.9: *Available data for the production cross sections of the reaction channel* $^{14}N(p,\alpha)^{11}C$*, in a range from 0 to 30 MeV. The data is provided by EXFOR.*

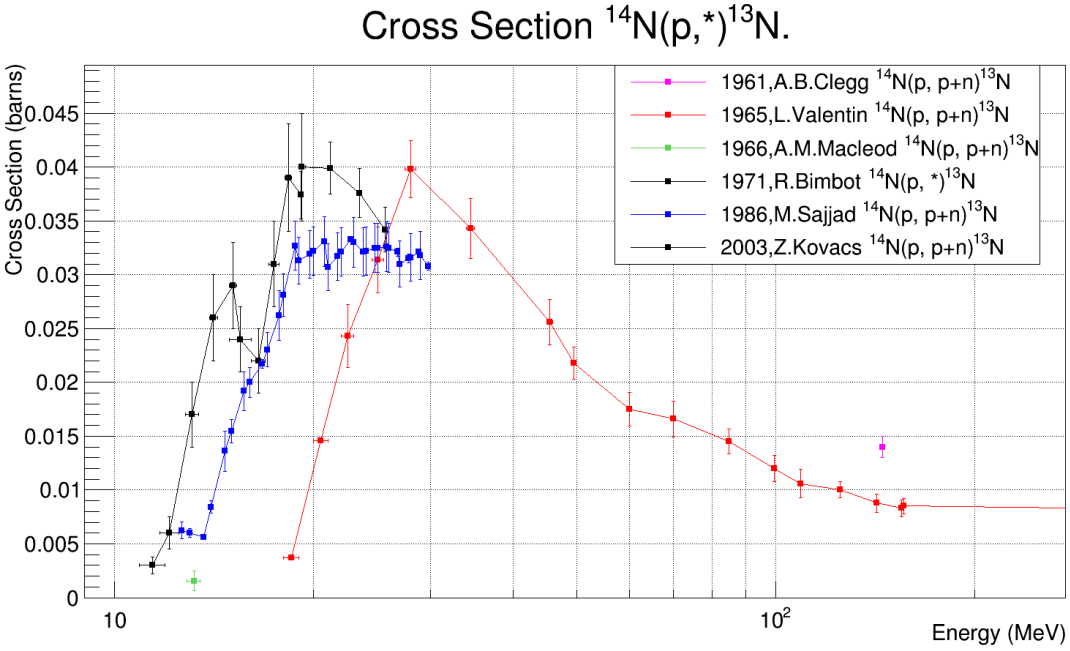

Figure 1.10: *Available data for the production cross sections of the reaction channel* $^{14}N(p,*)^{13}N$*, in a range from 0 to 160 MeV. The data is provided by EXFOR.*

1.6 Objectives

This work is part of a larger project aiming at measuring the production cross section of ^{11}C and ^{13}N in the full energy range of interest in protontherapy, up to 250 MeV. For this, it is necessary to develop and implement the experimental techniques in order to measure production cross sections of these nuclear reactions. As a first step, an experimental set up has been designed and tested at the 18 MeV cyclotron at CNA. These measurements at low energies are of interest on their own, as it is the energy near the end (last few millimetres) of the proton beam range.

The PET isotopes of interest are produced via the irradiation of ^{nat}C, ^{nat}N and ^{nat}O targets in the CNA cyclotron with a low-energy proton beam. These targets are made of a stack of thin films of the material of interest. In this way, production yields of these β^+ emitters can be measured for several energies at a same irradiation, considering that the proton beam goes through the films and in each of them the proton beam has a different energy. The activity curve is measured by a PET scanner to extract the number of positron emitters produced. As the PET scanner is outside the irradiation room, although oxygen is also produced in the irradiation, it has a half-life too short and we can not detect it before it fully decays. The irradiated targets used in this work are polyethylene (PE), Polymethyl-methacrylate (PMMA), Nylon-6, and the number of films used in each case has been calculated using the program SRIM, considering that it is convenient that the beam do not stop in order to measure the current beam.

The following step would be the measurement of these cross sections at higher energies taking into account the techniques, improvements and experimental set up developed in this work.

2. Experimental set-up: description and characterization

In order to measure the production cross section of ^{11}C and ^{13}N in ^{nat}C, ^{nat}N and ^{nat}O, three targets made of a stacks of thin films of PE, PMMA and Nylon-6 have been irradiated at the CNA cyclotron. In this way the energy of the proton traversing each film decreases from one film to the next. The activity induced in all films has been determined by measuring all of them simultaneously with the PET scanner at CNA.

This section describes the experimental set up and the measurements made to characterize both the cyclotron and the PET scanner.

2.1 18 MeV proton cyclotron at CNA

A cyclotron is a circular particle accelerator which, by the combined application of an oscillating electric field and a magnetic field, accelerates ions by spinning them in increasing radio-energy orbits. The one at CNA was the second particle accelerator, installed in 2004, and was manufactured by IBA (Belgium). It accelerates protons and deuterons to 18 and 9 MeV, respectively, with maximum beam intensities in the internal target ports of 80 μA for protons and 35 μA for deuterons. This accelerator has eight ports of irradiation, seven of them dedicated to the production of positron emitters for medical imaging and research, and the last one is an external line (Experimental Beam Line) used for research with the proton or deuteron beam.

The CNA cyclotron is sketched in figure 2.1. The first part is inside the cyclotron vault and it includes a retractable graphite Faraday cup, a variable graphite slit, a XY set of magnetic steerers and a doublet quadrupole. The second part is outside, separated from the other by a two meters thick wall, and it is equipped with a single quadrupole, a 15 mm diameter collimator, a pumping station and another Faraday cup with a phosphor scintillator in order to see the size and shape of the beam.

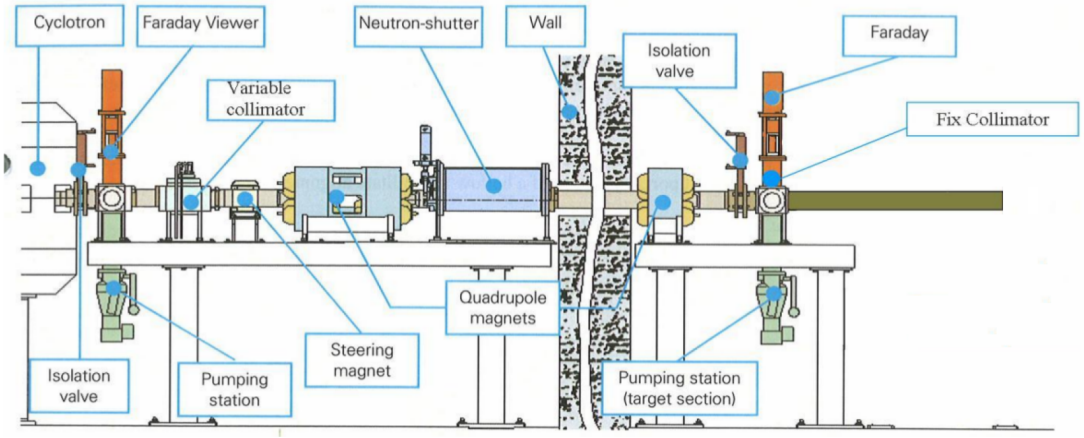

Figure 2.1: *Scheme of the cyclotron external line.*

Figure 2.2: *Left: 18 MeV (protons)/9 MeV (deuterons) cyclotron accelerator. Right: Experimental set-up, where one can see the sample holders with the different targets inside them, the external beam and the monitored table.*

In this work, a target holder has been designed and manufactured in order to place all the targets at the same time. As shown in figure 2.2, it is attached to a motorized table so that it can be remotely controlled. Using this system one can irradiate each stack of films without entering the experimental room between one irradiation and the rest, so that the decay of the induced activity is minimized.

In order to check the alignment and shape of the beam a stack of PMMA thin films was irradiated at high current. The beam produced a colouration of the targets, which were then scanned and analysed. The irradiated films are displayed in figure 2.3, where a 3D image of the color scale is shown in the right panel. The corresponding horizontal and

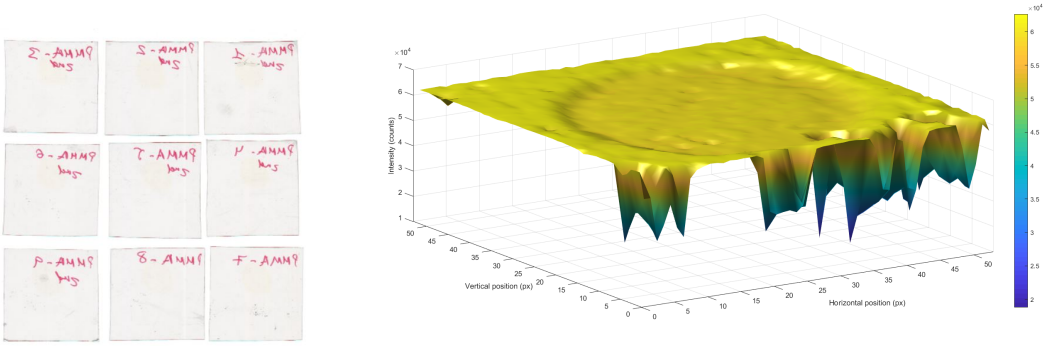

Figure 2.3: *Left: PMMA irradiated targets, which are scanned with a Epson Perfection V700 Photo Scanner. Right: Irradiation intensity of the PMMA-9 target.*

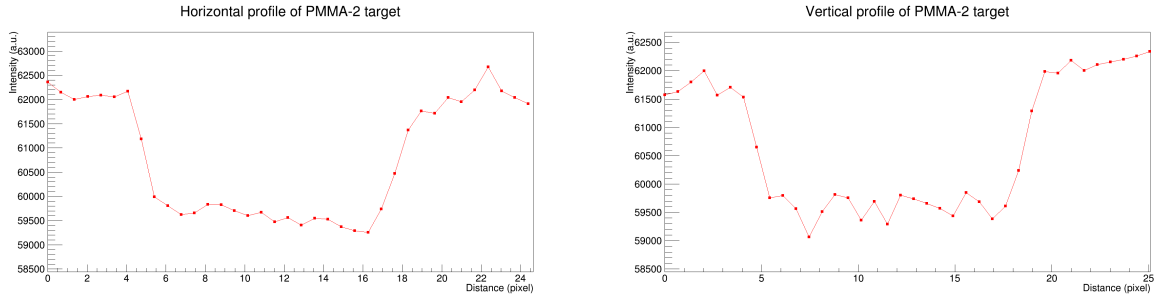

Figure 2.4: *Horizontal (left) and vertical (right) profile of the irradiation colouration in PMMA-9 target, for three different vertical positions. PMMA films are not radiochromic films and thus they can not measure the dose deposition profile, although they allow to measure the beam size.*

vertical projections (see figure 2.4) confirm the size of the beam (10 mm diameter of the collimator placed in the exit window) and serve to locate the beam centre, where the rest of the targets were placed and irradiated.

2.2 PET/CT scanner at CNA

Positron Emission Tomography – Computed Tomography (better known as PET/CT) is a nuclear medicine technique which combines, in a single equipment, a positron emission tomography scanner and an X-ray computed tomography (CT) scanner. It can acquire sequential images from both devices in the same session, and combine them into a single superposed image. Thus, functional imaging obtained by PET, which depicts the spatial distribution of metabolic or biochemical activity in the body can be more precisely aligned with the anatomic image obtained by CT scanning.

Figure 2.5: *PET/CT Scanner at the CNA facilities.*

The PET system detects pairs of 511 keV γ-rays in coincidence, emitted in the annihilation of a positron produced in the β^+-decay of a radionuclide (tracer). The radionuclide is introduced into the body on a biologically active molecule, such as fludeoxyglucose (FDG), and the concentration of the tracer imaged indicates where the glucosa has been uptaken by the tumor cells.

In 2011, the National Accelerator Centre (CNA) acquired a PET/CT for humans (figure 2.5) aiming at both clinical and research activities. It is a Siemens Biograph mCT with PET detectors with a 162 mm axial field of view, and CT detectors that allow obtaining 64-slices images. The PET scanner, made of 144 Lutetium Oxyorthosilicate (LSO) scintillator with 4 photomultiplier tubes each, looks for coincident γ-rays depositing energy between 425 and 650 keV within a time window of only 4.5 ns. The radioactive isotope ^{176}Lu (β^- with a half-life of $3.78{\cdot}10^{10}$ years) amounting to 2.6% of the natural lutetium present in LSO emits electrons with a mean energy of 420 keV. In addition, it emits three γ-rays of 88, 202, and 307 keV simultaneously to the β^- particle [24]. This results in an intrinsic background of the PET scanner.

In this work, the PET/CT scanner works as a multi-detector operating in coincidence in order to measure the activity of irradiated targets placed inside the PET/CT and then obtain the cross sections of interest. For the purpose of this work, the PET/CT has a

Position		PROPCPS		
^{22}Na – 1	^{22}Na – 2	^{22}Na – 1	^{22}Na – 2	Conversor
1.1	1.4	3368	21106	–
1.4	4.1	3601	20071	–
4.2	1.2	3141	18385	–
1.1	1.4	3555	21542	PE
1.4	4.1	3238	21397	PE
4.2	1.2	3462	19191	PE

Table 2.1: PROPCPS of the different β^+ sources, measured in several positions during ten minutes.

Position		PROPCPS		
^{22}Na – 1	^{22}Na – 2	^{22}Na – 1	^{22}Na – 2	Time
1.1	1.4	3247	20586	2 min
1.1	1.4	3290	20663	2 min
1.1	1.4	3339	20519	2 min
1.1	1.4	3368	21106	10 min
1.1	1.4	3406	21167	10 min
1.1	1.4	3392	21049	10 min

Table 2.2: PROPCPS of the different β^+ sources, measured in a fixed positions during two and ten minutes. The conversor is polyethylene.

considerable advantage over a simple scintillator detector, because there is a great number of films to measure and its good spacial resolution allows measuring all the targets at the same time.

A protocol of reconstruction (such as time of flight, true X or iterative reconstruction) is necessary to transform the PET data into the number of 511 keV photons emitted by each target. In addition, a correction by attenuation is used to correct for the fact that the photons go through different materials before reaching the detector. The result is a 3D map in units of PROPCPS (proportional to counts per second), that is then transformed into unity of activity using a calibrated source of ^{22}Na.

PET scanners for medical imaging do not require a very accurate efficiency calibration, neither in absolute value nor in its dependency with the position. Therefore, several ex-

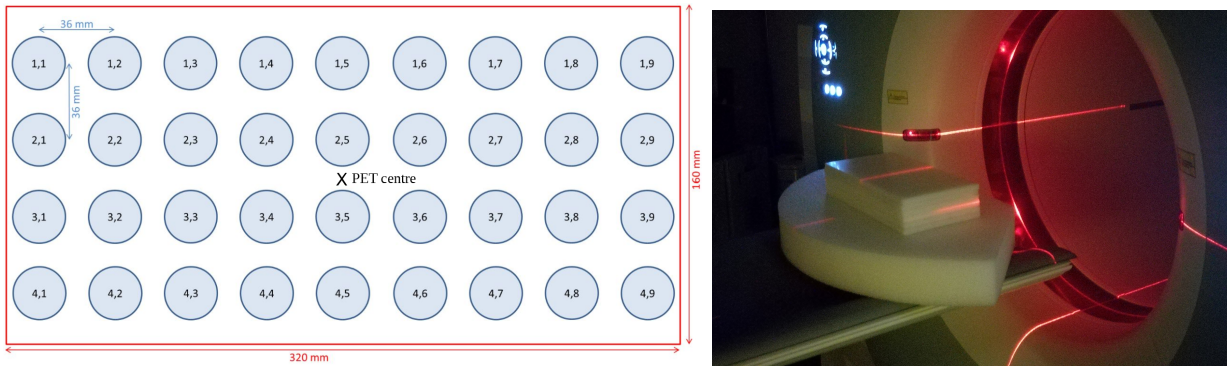

Figure 2.6: *Left: Template of the polyethylene sheet built for the emplacement of the ^{22}Na source. Right: PET/CT scanning system and set up of the polyethylene sheets covering the sample.*

periments were carried out before the measurement of the irradiated targets in order to test the PET scanner spatial efficiency and statistic uncertainty.

In a first step two ^{22}Na sources with different activities (124 kBq for ^{22}Na-1 and 803 kBq for ^{22}Na-2) where measured at three different positions (see figure 2.6), with and without a surrounding material (see table 2.1). The results show that the PROPCPS values vary around 5-6% depending on the position of the source. This confirms the need for a spatial calibration of the PET. In a second step (see table 2.2), the number of PROPCPS for both ^{22}Na sources is measured during different acquisition times in order to estimate the statistical uncertainty of the measurements. Acquisitions of 2 minutes provide a 1% statistical uncertainty, and 0.5% for 10 minutes acquisitions. Since the aimed accuracy for the detection efficiency is $\sim$2% we have taken 1 minute measurements of the ^{22}Na (see below).

The PET efficiency as function of the position has been determined by looking at a ^{22}Na source placed at 36 (9x4) different positions on two horizontal planes, using a polyethylene matrix similar to that of the measurements of the irradiated films (see sketch in figure 2.6). The alignment was made using the laser positioning of the PET room.

In total, six polyethylene sheets of $32\times16\times1$ cm^3 were used. Four of them without any hole, and two of them with 9×4 holes, separated 36 mm, in order to place the source inside them, and acquire the number of PROPCPS during a minute.

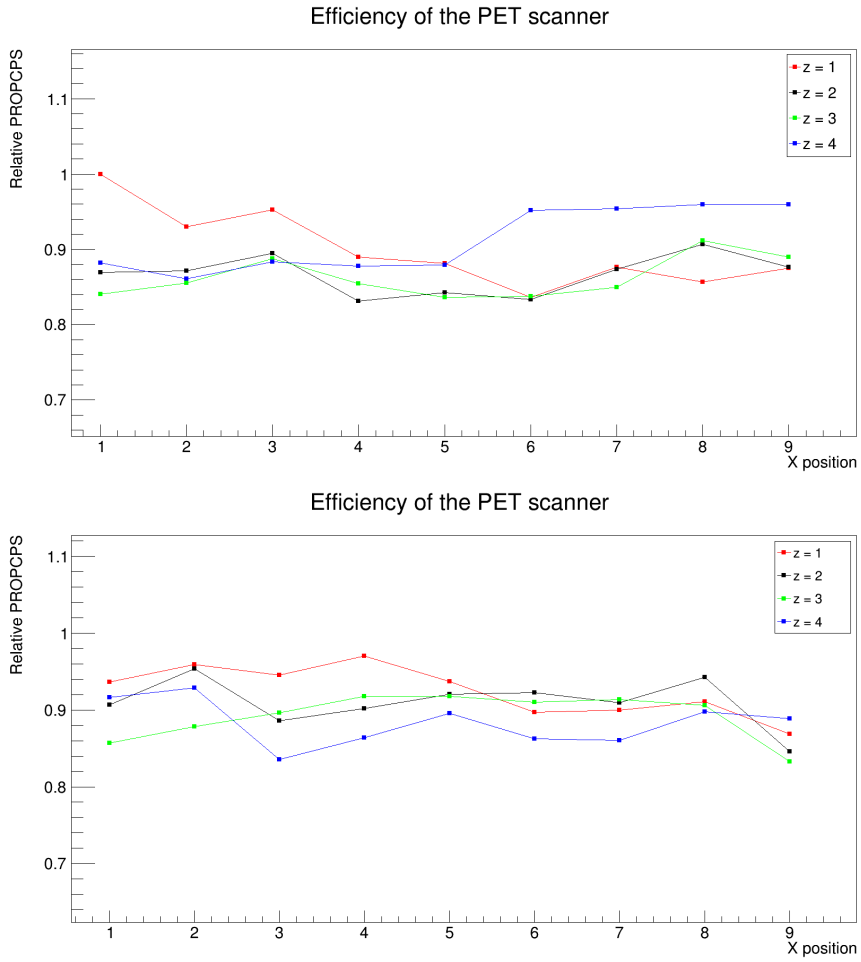

Figure 2.7: *Spatial calibration in efficiency for each position.*

The results (figures 2.7 and 2.8) show efficiency variations in the order of 5-10% with the positions, being fairly constant at the centre of the PET. In figure 2.7, one can se that the z=1 and z=4 curves are opposed to each other, with differences in efficiency between the edges and the centre of around 10%. This can be explained because the polyethylene matrix was not completely lined up in the x axis, so opposite corners have the same behaviour: two of them are close to the centre and the others are close to the extremes, therefore the solid angle coverage is different in each case. Moreover, the z=2 and z=3 have a similar behaviour, and all the curves are approximately constant (within 4%) in the centre of the polyethylene sheets.

In this way the efficiency in the PET scanner has been determined in all the different

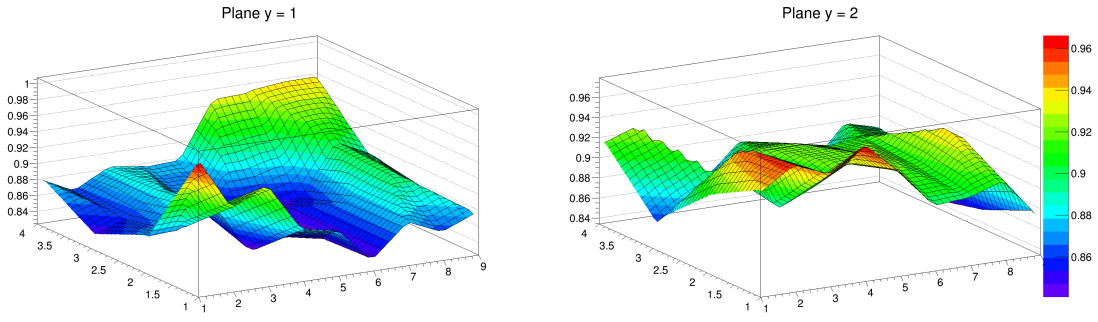

Figure 2.8: *3D representation of the PET scanner efficiency, for plane y=1 (left) and plane y=2 (right).*

positions in which the irradiated targets will be placed within an uncertainty of 2%.

2.3 Target configuration for irradiation

The energy of the beam provided by the cyclotron is fixed to 18 MeV, but the aim of this experiment is to measure the production cross sections at different energies below 18 MeV. For this, the targets were made of a stack of thin films in such a way the energy of the protons traversing each film is decreasing from one to the next. The number of films in each target were chosen so that the total thickness is not enough to stop the beam. In this way the beam current can be monitored and measured with a beam dump after the targets.

The materials chosen to measure reactions in C, N and O are polyethylene (PE), polymethylmethacrylate (PMMA) and polycaprolactam (Nylon-6), all supplied by Goodfellow. The characteristics of the targets are given in table 2.3. The thickness of the films were measured by weighting pieces of known surface, obtaining the values listed in table 2.3. While the values for PE and PMMA agree with those from the provider, the one of Nylon-6 was found to be 76(1) μm instead of the 100 μm claimed by the provider (with a tolerance of 20%).

The energy of the beam before and after each film is calculated using SRIM-2013 [23]: group of programs which calculate the stopping and range of ions (up to 2 GeV/amu) into matter using a quantum mechanical treatment of ion-atom collisions (assuming a moving atom as an "ion", and all target atoms as "atoms"). This calculation is made very efficiently

Material	Density (g/cm^3)	Composition	Number of layers	Provided thickness (μm)	Measured thickness (μm)
PE	0.96	$(C_2H_4)_n$	12	200($\pm$20%)	198(2)
PMMA	1.18	$(C_5O_2H_5)_n$	9	250($\pm$20%)	247(3)
Nylon-6	1.13	$(C_6H_{11}N_O)_n$	20	100($\pm$20%)	76(1)

Table 2.3: Target configuration for the irradiation. The uncertainty in the thickness was estimated of the standard deviation of three independent measurements. The geometry of the films is square (40×40 mm^2).

by the use of statistical algorithms which allow the ion to make jumps between calculated collisions and then averaging the collision results over the intervening gap. SRIM provides the proton beam energy distribution after traversing each target, taking into account that there is a 100 μm Al window in the exit of the cyclotron line and that the proton beam travels 51 mm in air before reaching the first target. Then, the average energy inside each target can be obtained as (see figure 2.9)

$$\bar{E} = \frac{\bar{E}_{in} + \bar{E}_{out}}{2}, \tag{2.1}$$

where $\bar{E}_{in}$ and $\bar{E}_{out}$ are the incident average energy and the outgoing average energy in each target. The energy spread of the beam in each target is calculated as:

$$\delta E_{low} = \frac{FWHM_{out}}{2} + \frac{\bar{E}_{in} - \bar{E}_{out}}{2}, \tag{2.2}$$

and

$$\delta E_{high} = \frac{FWHM_{in}}{2} + \frac{\bar{E}_{in} - \bar{E}_{out}}{2}, \tag{2.3}$$

where $FWHM_{out}$ and $FWHM_{in}$ are the full widths at half maximum of the gaussian fit in each simulated energy distribution. The results for the three target materials are shown in figure 2.10.

Therefore, the total number of energy points depends on the number of films used. In PE films the energy range covers from 17.0 MeV to 8.6 MeV, increasing the spread in energy from 2% to 9%, respectively. In the PMMA films, the production cross section is measured from 3.6 MeV with an energy uncertainty of the 60% up to 16.1 MeV with a

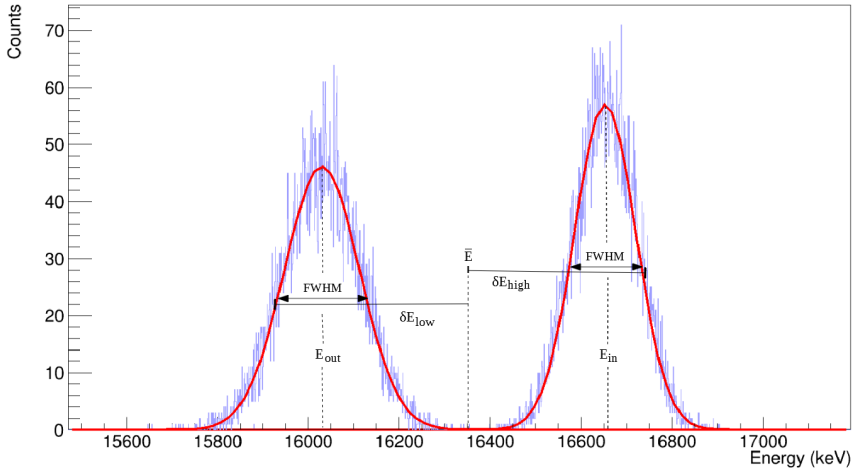

Figure 2.9: *Example of the entering and exiting proton beam in PE-2 target.*

uncertainty of 4%. Finally, in Nylon-6 targets the number of energy points is larger, with the production cross sections measured from 7.9 MeV (uncertainty of 8%) to 16.5 MeV (uncertainty of 2%).

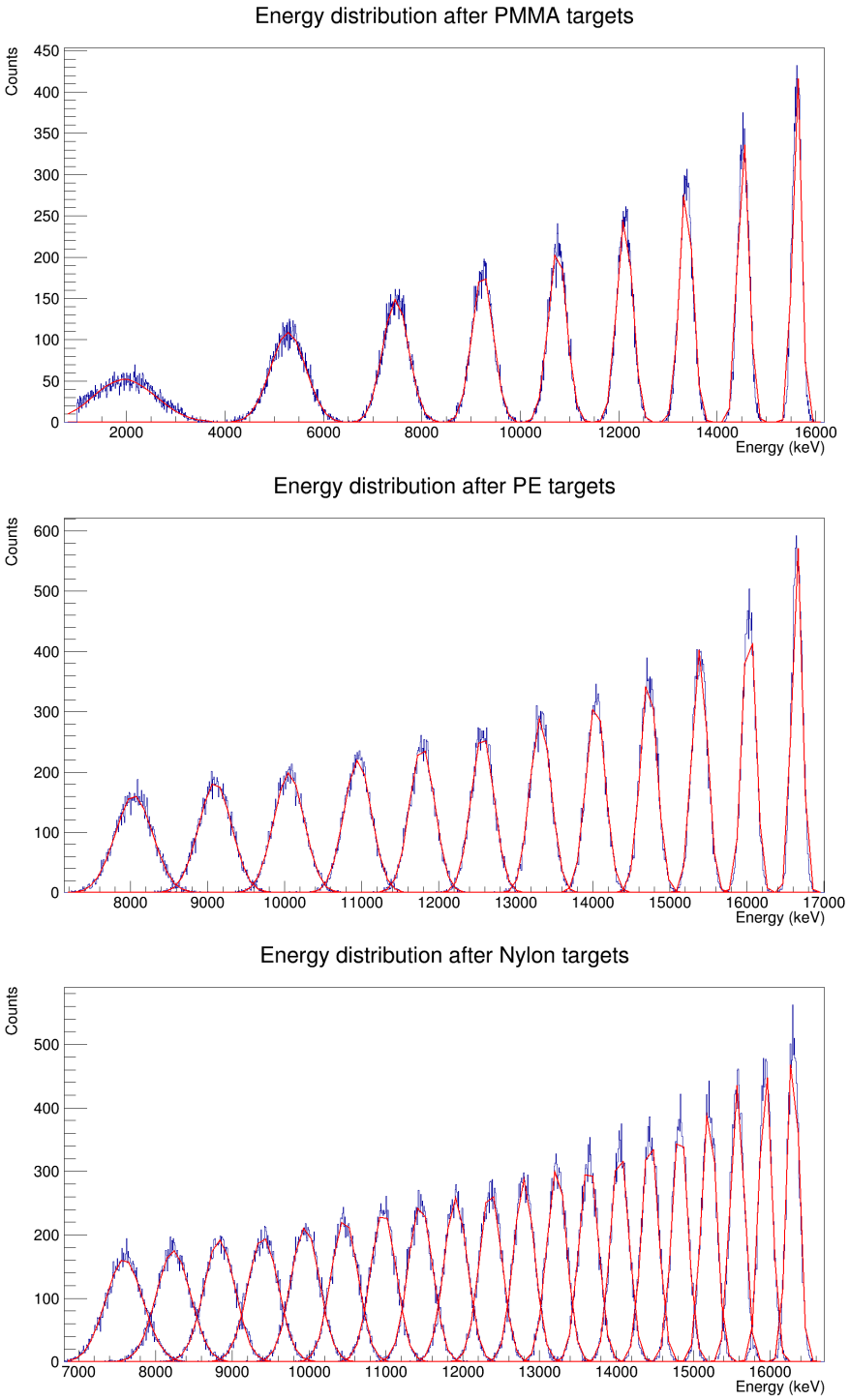

Figure 2.10: *Energy distribution after the proton beam traverse each target. The blue line is the number of protons in each energy interval and the red line is the gaussian fitting curve.*

3. Experiments at CNA, analysis and results

The experiment consisted in the irradiation of the different targets at the 18 MeV cyclotron and the subsequent quantification (measuring with the PET scanner) of the activity induced in each film. This has been then translated into the corresponding reaction cross sections.

3.1 Irradiation and PET measurement

Four irradiations were carried out with the configurations summarized in table 3. The scintillator was irradiated first to verify visually the alignment of the beam. For this and the other three stacks of films, a polyethylene film was placed in the first position. As it will be discussed later, the activity induced in this first film serves to verify the measured beam current.

The beam current during the irradiation is monitored using as beam dump an electrically isolated graphite (placed after the targets) connected to a Brookhaven 1000c Current Integrator. The total charge is calculated taking into account the secondary electron losses in graphite characterized in a previous work by biasing a graphite target into a vacuum chamber. Table 3.1 summarizes the duration of each irradiation, the total incident charge in each target and the time offset between the end of the irradiation (EOI) and the start of the PET acquisition.

It is seen in table 3.1 that the PMMA measurement was performed later than the others. Actually, in a first irradiation of PMMA the films were damaged due to high current and thus a second irradiation of a new target was done for a longer time using a reduced beam current. This reduced beam current was also used for the scintillator, as it can be seen in figure 3.1. This figure shows the current (left) and accumulated charge (right) as function of the irradiation time. One can see that the flux of protons was constant during the irradiation of the PE, Nylon-6 and scintillator targets. However, in the case of PMMA targets, the measured current fluctuates in the last minutes of the irradiation. A possible explanation is that the samples started to damage towards the end of the irradiation.

Irradiation	PE	PMMA	Nylon	Scintillator
Irradiation time	4' 5"	11' 40"	4' 19"	9' 54"
Time offset	36' 10"	21' 24"	51' 59"	36' 13"
PET acq. time	5h	3h 52'	5h	3h 52'
Total charge	8.7(4)μC	8.7(4)μC	8.7(4)μC	6.5(3)μ
Number of targets	12	1 PE + 9	1 PE + 20	1 PE

Table 3.1: Experimental configuration during irradiation and PET/CT detection.

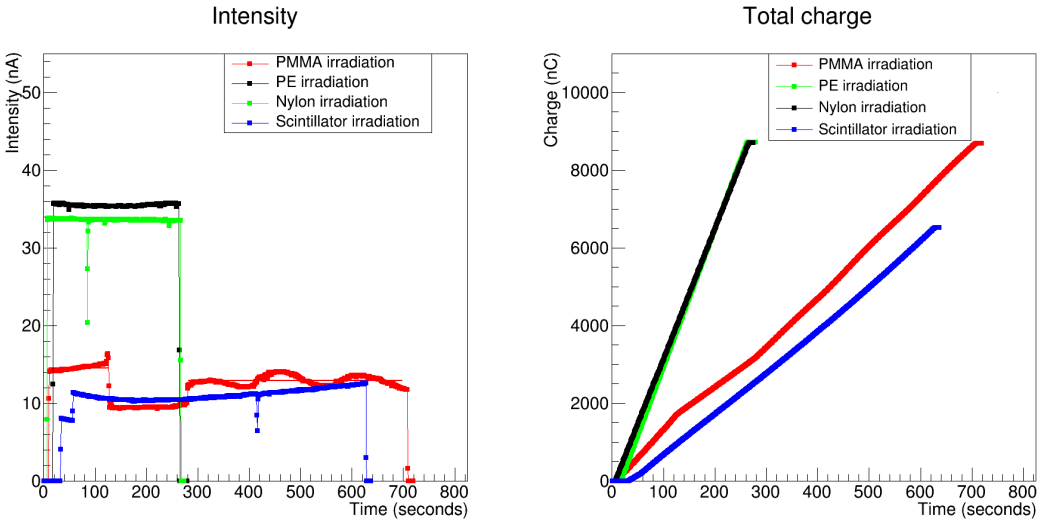

Figure 3.1: *Current beam measured in a graphite, for each irradiation, as well as the total charge.*

The irradiated targets were placed inside a PE matrix acting as a conversor of the positron into a couple of 511 keV photons. The matrix and the target therein are shown in figure 3.2. There are 36 mm distance between each target in the horizontal (x-z) plane, and 4 cm distance in the vertical (y) plane. The images from the PET/CT scanner are shown in figure 3.3. In order to measure the activity in each film, a spherical volume of interest (VOI) of 3 cm in diameter is defined for each position. A total of 42 VOIs have been studied. Using a dynamic analysis of the PET images, where the reconstruction technique is TrueX and correction by attenuation, the result is the PROPCPS in each VOI in time intervals of one minute. The decay time has been corrected by the time offset and the PROPCPS values converted into activity using as reference a ^{22}Na (124±7 kBq) source

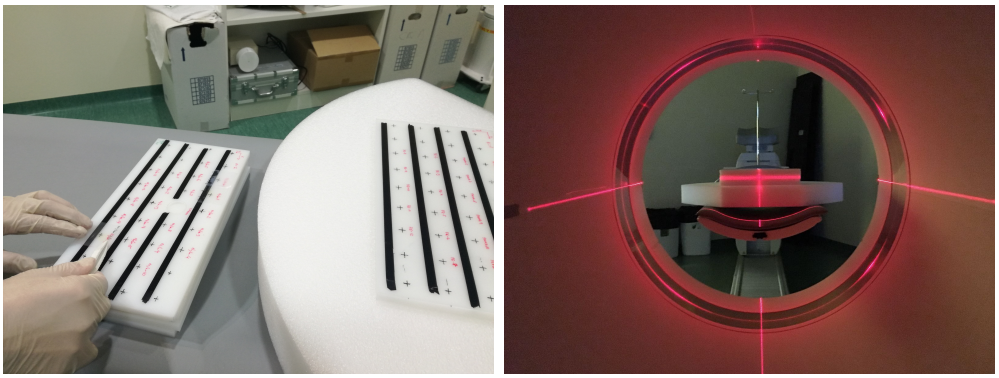

Figure 3.2: *Polyethylene matrix with irradiated targets inside the PET scanner.*

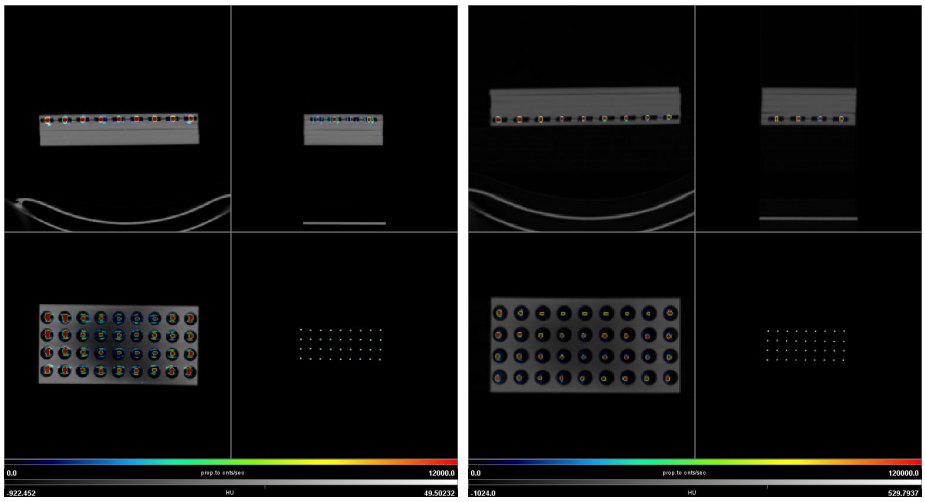

Figure 3.3: *PET images superposed to CT image in the three planes, for y=1 and y=2.*

placed at the position (5,2,2). The activity of the ^{22}Na calibration source was verified within 8% using an activimeter at CNA. The results are the activity curves discussed in the following.

3.2 Fitting activity curves

The activity curves have been obtained taking into account the PET spatial resolution and a correction due to the decay during the irradiation time, in order to have the total production yield as a function of the initial activity. The production yield in case a nucleus decays is

$$\frac{dN}{dt} = -\lambda N + f_{production}, \tag{3.1}$$

	$r_{^{11}C}$	$r_{^{13}N}$
PE irradiation	1.07	1.14
PMMA irradiation	1.21	1.46
Nylon irradiation	1.08	1.16

Table 3.2: Correction factor by decay during the irradiation.

where λ is $ln(2)/T_{1/2}$ and $f_{production}$ is proportional to the cross section. Then,

$$\frac{dN}{dt} = -\lambda N + n\sigma I, \tag{3.2}$$

where n is the number of atoms per unity of area of the irradiated material and I is the flux of incident particles. Solving this differential equation, taking into account that $N(0) = 0$ and $N(T_{irrad}) = A_0/\lambda$:

$$N_{decay} = n\sigma I\lambda^{-1}(1 - e^{-\lambda T_{irrad}})e^{-\lambda t}, \tag{3.3}$$

where T_{irrad} is the irradiation time of each stack of targets. On the other hand, assuming that the nuclei do not decay during the irradiation, i.e., the time of irradiation is much smaller than the half-life of the isotope, then

$$N_{nodecay} = n\sigma I T_{irrad}, \tag{3.4}$$

Thus, the ratio between the production yield assuming the realistic and the "no decay" cases, is:

$$r = \frac{\lambda T_{irrad}}{1 - e^{-\lambda T_{irrad}}}. \tag{3.5}$$

Therefore, one must correct by this factor for each initial activity obtained, in order to have the real production yields when the irradiation ended. Table 3 summarizes the correction factor for the production yields of the different irradiations. The production yield of ^{13}N is significantly more affected than ^{11}C, due to the fact that the ^{13}N half-life is shorter than that of ^{11}C.

As mentioned before, a PE film was placed in the first position for each stack of targets. The analysis of the corresponding activity curves, displayed in figure 3.4, shows that the activity curves corrected by the decay time during the irradiation and normalized to the

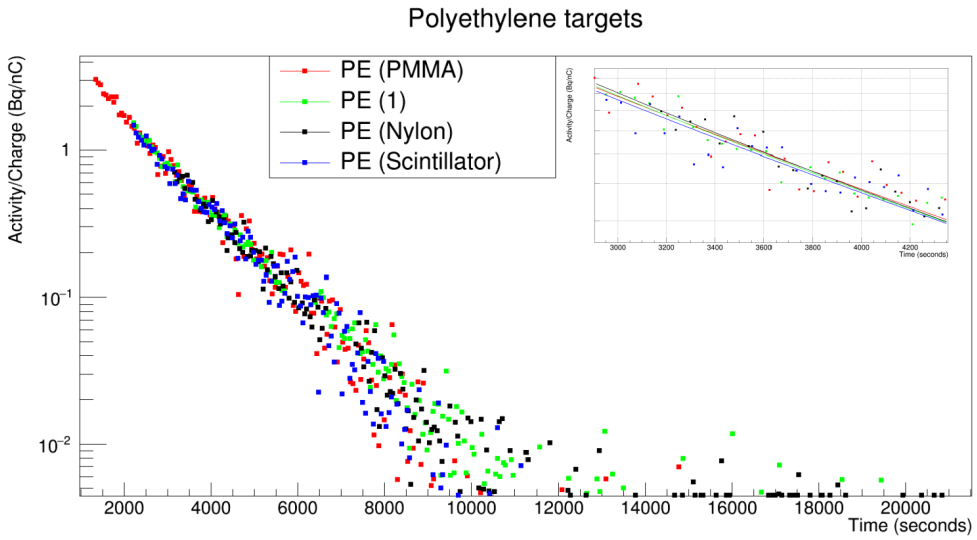

Figure 3.4: *Activity curve in function of time in the first PE film of each set of targets.*

total charge agree within 8%. The difference between each fit (2-8%) is compatible with the uncertainty in the current beam (5%). It allows to validate the monitoring of the current beam, even in PMMA targets (see figure 3.1, left).

The activity curves of all films have been analysed making use of the ROOT software whose algorithms are based on the minimum chi-squared method. Taking into account the decay constant of ^{11}C and ^{13}N, and the background introduced by the ^{22}Na source and ^{176}Lu present in the LSO scintillator crystals, the activity curves are fitted to the following expression:

$$f(t) = A_0 + A_{^{11}C} e^{-\lambda_{^{11}C} t} + A_{^{13}N} e^{-\lambda_{^{13}N} t}, \tag{3.6}$$

where $A_{^{11}C}$ and $A_{^{13}N}$ are the activities at EOI of the isotopes ^{11}C and ^{13}N, respectively, with $\lambda_{^{11}C} = ln(2)/T_{1/2}^{^{11}C}$ and $\lambda_{^{13}N} = ln(2)/T_{1/2}^{^{13}N}$. The half-life of the ^{11}C and ^{13}N are 20.36 and 9.967 min, respectively. The figures 3.5, 3.6 and 3.7 show the result of the fitted activation curves in each film. The blue line represents the fitted activity of ^{13}N, the green line represents the activity curve of ^{11}C and the red line the total fit, including background. The results of the fits are summarized in tables 3.4, 3 and 3.5, which contain the results for the activities at EOI corrected by the decay factor r as function of the proton beam energy.

The total uncertainty of these results has contribution from the uncertainty in the fitting curve (as given by ROOT), the PET scanner efficiency dependence with the position (2%), the measurement of the beam current (estimated to be 5%), the uncertainty in the activity of the calibration source (1%) and the uncertainty in the target thickness (1%). The total relative uncertainty is calculated as the square root of the sum of squares of the partial uncertainties.

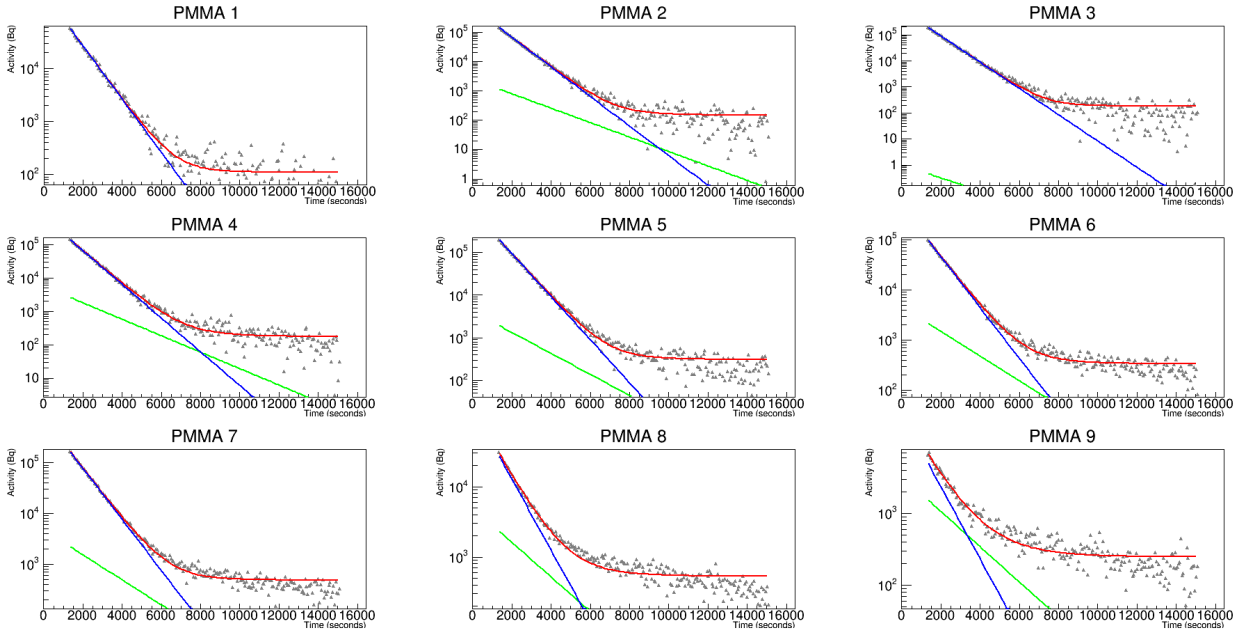

Figure 3.5: *Fitted activity curve in PMMA targets. The blue line represents the fitted activity of* ^{13}N*, the green line represents the activity curve of* ^{11}C *and the red line the total fit, including background.*

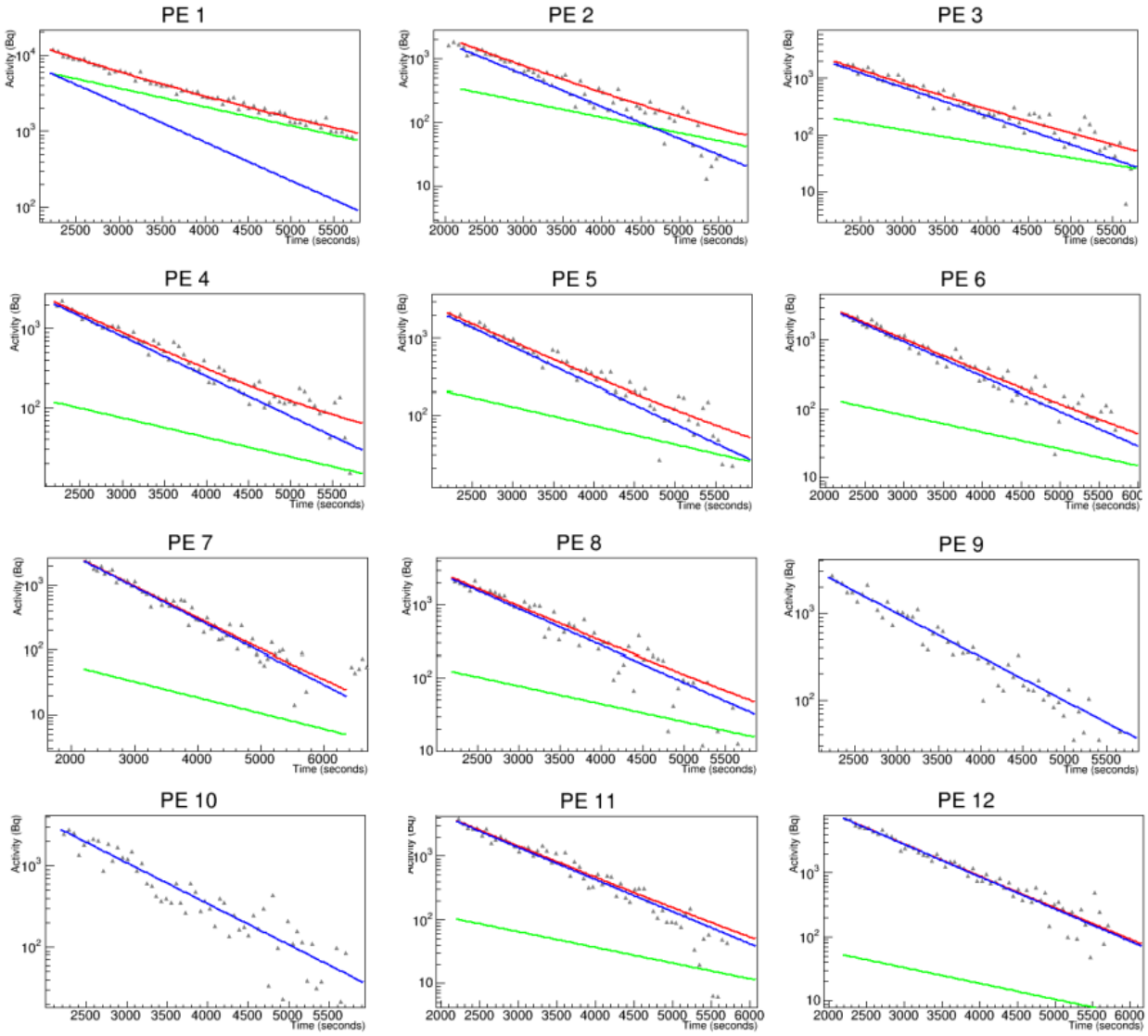

Figure 3.6: *Fitted activity curve in PE targets. The blue line represents the fitted activity of ^{13}N, the green line represents the activity curve of ^{11}C and the red line the total fit, including background.*

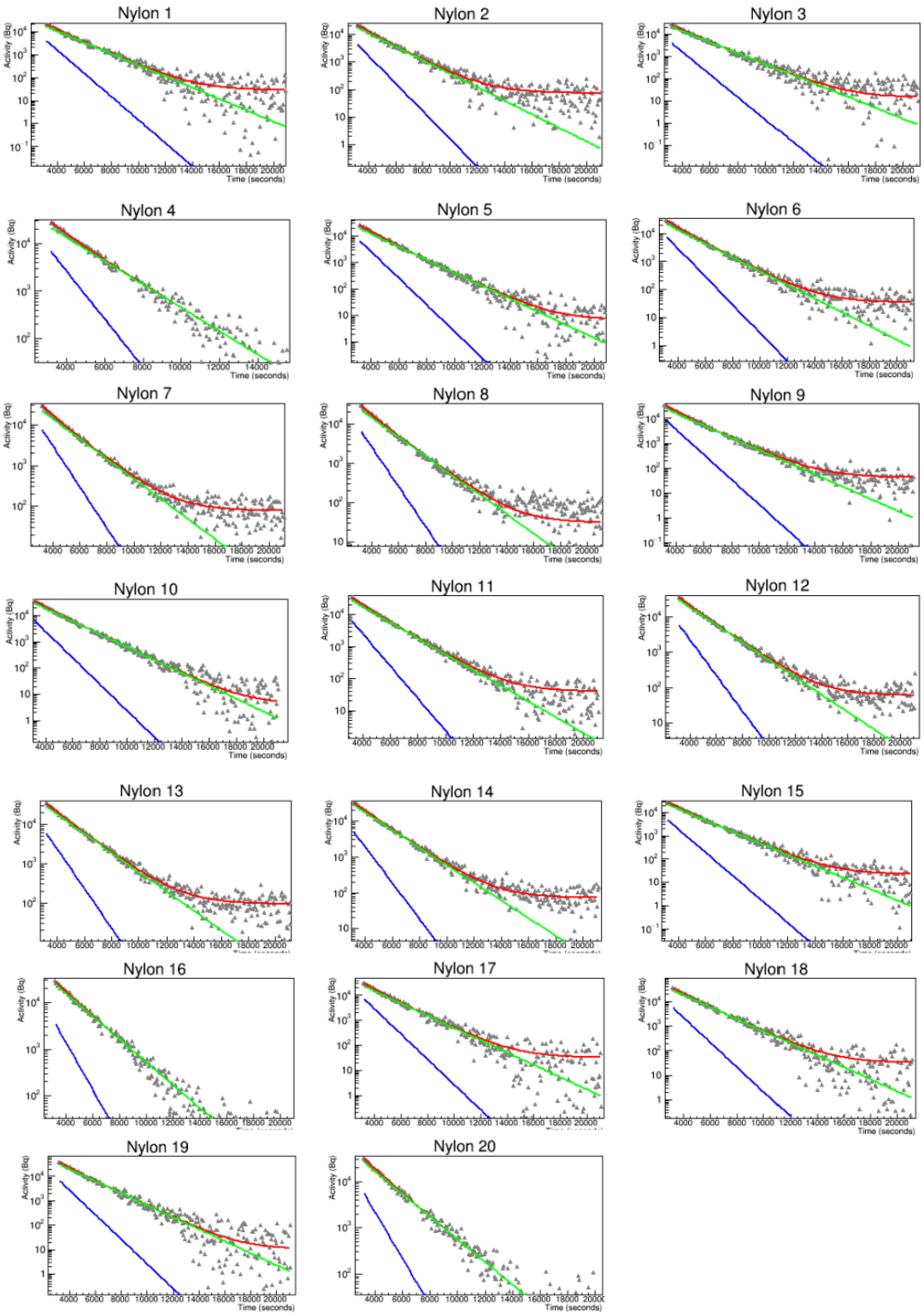

Figure 3.7: *Fitted activity curve in Nylon-6 targets. The blue line represents the fitted activity of* ^{13}N*, the green line represents the activity curve of* ^{11}C *and the red line the total fit, including background.*

Energy (MeV)	$A_{^{11}C}$ (kBq)	$A_{^{13}N}$ (kBq)
$17.0^{+0.4}_{-0.4}$	21 ± 3	86 ± 11
$16.3^{+0.4}_{-0.4}$	1 ± 3	21 ± 3
$15.7^{+0.4}_{-0.4}$	0.73 ± 0.05	26 ± 4
$15.1^{+0.4}_{-0.5}$	0.44 ± 0.03	30 ± 3
$14.4^{+0.5}_{-0.5}$	0.75 ± 0.08	28 ± 4
$13.7^{+0.5}_{-0.5}$	0.48 ± 0.03	35 ± 3
$13.0^{+0.5}_{-0.6}$	0.190 ± 0.011	35 ± 3
$12.2^{+0.6}_{-0.6}$	0.46 ± .03	33 ± 3
$11.4^{+0.6}_{-0.6}$	*	37.3 ± 2.4
$10.5^{+0.7}_{-0.7}$	*	41 ± 3
$9.6^{+0.7}_{-0.7}$	0.380 ± 0.023	51 ± 4
$8.6^{+0.8}_{-0.8}$	0.193 ± 0.012	104 ± 7

Table 3.3: Initial activity in each target of PE. (*) The results of these fit are too small and can not be trusted data, due to the low production yield of 11C in PE targets.

Energy (MeV)	$A_{^{11}C}$ (kBq)	$A_{^{13}N}$ (kBq)
$16.1^{+0.6}_{-0.6}$	0.1 ± 1.4	401 ± 24
$15.1^{+0.7}_{-0.7}$	3.0 ± 1.6	990 ± 60
$14.0^{+0.7}_{-0.7}$	$(1.2 \pm 0.8)\cdot 10^{-3}$	1350 ± 80
$12.7^{+0.8}_{-0.8}$	6.8 ± 1.5	970 ± 60
$11.4^{+0.9}_{-0.9}$	5.0 ± 1.6	1380 ± 80
$10.0^{+1.0}_{-1.0}$	5.6 ± 1.0	670 ± 40
$8.4^{+1.1}_{-1.2}$	5.7 ± 1.4	1160 ± 70
$6.4^{+1.4}_{-1.5}$	6.0 ± 0.7	188 ± 11
$3.6^{+2.1}_{-2.6}$	4.0 ± 0.4	35 ± 2

Table 3.4: Initial activity in each target of PMMA.

Energy (MeV)	$A_{^{11}C}$ (kBq)	$A_{^{13}N}$ (kBq)
$16.5^{+0.3}_{-0.3}$	108 ± 7	184 ± 18
$16.1^{+0.3}_{-0.3}$	117 ± 7	203 ± 21
$15.8^{+0.3}_{-0.3}$	142 ± 9	188 ± 22
$15.4^{+0.3}_{-0.3}$	138 ± 9	310 ± 30
$15.0^{+0.3}_{-0.3}$	128 ± 8	314 ± 23
$14.6^{+0.3}_{-0.3}$	144 ± 9	360 ± 30
$14.2^{+0.3}_{-0.3}$	144 ± 9	359 ± 25
$13.8^{+0.3}_{-0.4}$	149 ± 9	306 ± 24
$13.4^{+0.4}_{-0.4}$	166 ± 10	430 ± 30
$13.0^{+0.4}_{-0.4}$	194 ± 12	292 ± 22
$12.6^{+0.4}_{-0.4}$	179 ± 11	296 ± 22
$12.1^{+0.4}_{-0.4}$	192 ± 12	273 ± 21
$11.7^{+0.4}_{-0.4}$	186 ± 11	282 ± 23
$11.2^{+0.4}_{-0.4}$	179 ± 11	227 ± 23
$10.7^{+0.4}_{-0.5}$	150 ± 9	235 ± 20
$10.2^{+0.5}_{-0.5}$	160 ± 10	160 ± 23
$9.7^{+0.5}_{-0.5}$	153 ± 9	340 ± 30
$9.1^{+0.5}_{-0.5}$	194 ± 12	270 ± 30
$8.5^{+0.5}_{-0.6}$	205 ± 13	320 ± 30
$7.9^{+0.6}_{-0.6}$	173 ± 11	264 ± 24

Table 3.5: Initial activity in each target of Nylon.

3.3 Production yields and cross sections

The production yield of the isotope i during the irradiation of the target k is given by

$$\frac{dN_i^k}{dt} = \sum_j p_j n_j^k \sigma_{j\to i} I_k, \tag{3.7}$$

	H (atoms/cm^2)	C (atoms/cm^2)	O (atoms/cm^2)	N (atoms/cm^2)
PE	$1.62 \cdot 10^{21}$	$8.09 \cdot 10^{20}$	0	0
PMMA	$1.43 \cdot 10^{21}$	$8.96 \cdot 10^{20}$	$3.58 \cdot 10^{20}$	0
Nylon	$6.62 \cdot 10^{20}$	$3.61 \cdot 10^{20}$	$6.02 \cdot 10^{19}$	$6.02 \cdot 10^{19}$

Table 3.6: Targets composition.

where p_j is the abundance of the isotope j, n_j^k is the number of nuclei of the j element in k-target per unity of area, I_k is the flux of incident protons in k-target in particles per unity of time, and $\sigma_{j\to i}$ is the production cross section of element i. Since production yield can be related with activity by means of $N = A/\lambda$, then one has

$$\frac{dA_i^k}{dt} = \sum_j \lambda_i p_j n_j^k \sigma_{j\to i} I_k. \tag{3.8}$$

The solution of this differential equation is

$$A_i^k = \sum_j \lambda_i p_j n_j^k \sigma_{j\to i} I_k T_{irrad}, \tag{3.9}$$

and making use of $I_k T_{irrad}^k = C_k/|e|$, where C_k is the total charge accumulated in k-target and e is the charge of the electron, the activity at EOI produced is, excluding the decay:

$$A_i^k = \sum_j \lambda_i p_j n_j^k \sigma_{j\to i} \frac{C_k}{|e|}. \tag{3.10}$$

Consequently, the production cross section can be written in terms of the decay constant, the initial activities, the total charge accumulated during the irradiation, the number of atoms of each element and its relative abundance. The abundance of the isotope ^{12}C is 98,9%, whereas for the isotope ^{13}C is the 1,1%. Moreover, the isotopic relative abundance of ^{16}O and ^{14}N is 0,998% and 0,996%, respectively. The number of atoms of each isotope in the different materials are calculated using the density of the material and its thickness. The results are summarized in table 3.6.

Since, the production cross section of ^{11}C and ^{13}N in the PE films involves only carbon

atoms ($p_{^{12}C} + p_{^{13}C} = 1$), the cross section can be written simply as

$$\sigma_{C_{nat}\to i} = \frac{A_i^{PE} \cdot |e|}{\lambda_i \cdot n_{C_{nat}}^{PE} \cdot C_{PE}}, \tag{3.11}$$

where A_i^{PE} is the initial production activity in PE targets for each one of the positron emitters produced.

However, since PMMA and Nylon-6 contain also oxygen and nitrogen, different reaction channels can contribute to the production of ^{11}C and^{13}N. Therefore, both carbon and oxygen contribute to the production of positron emitters ^{11}C and^{13}N in PMMA targets, whereas carbon, oxygen and nitrogen contribute to the production in Nylon targets.

Therefore, the production cross section in ^{nat}C obtained from the analysis of the PE targets is subtracted from the ones in PMMA in order to obtain the cross section in oxygen:

$$\sigma_{O_{nat}\to i} = \frac{A_i^{PMMA} \cdot |e|}{\lambda_i \cdot p_{^{16}O} \cdot n_{O_{nat}}^{PMMA} \cdot C_{PMMA}} - \frac{n_{C_{nat}}^{PMMA} \cdot \sigma_{C_{nat}\to i}}{p_{^{16}O} \cdot n_{O_{nat}}^{PMMA}}, \tag{3.12}$$

where A_i^{PMMA} is the initial production activity in PMMA targets for each one of the positron emitters produced. Similarly, in order to obtain the production cross section of natural nitrogen, one must subtract the contribution of carbon and oxygen producing the positron emitters ^{11}C and^{13}N:

$$\sigma_{N_{nat}\to i} = \frac{A_i^{Nylon} \cdot |e|}{\lambda_i \cdot p_{^{14}N} \cdot n_{N_{nat}}^{Nylon} \cdot C_{Nylon}} - \frac{n_{C_{nat}}^{Nylon} \cdot \sigma_{C_{nat}\to i}}{p_{^{14}N} \cdot n_{N_{nat}}^{Nylon}} - \frac{n_{O_{nat}}^{Nylon} \cdot \sigma_{O_{nat}\to i}}{p_{^{14}N} \cdot n_{N_{nat}}^{Nylon}}, \tag{3.13}$$

where A_i^{Nylon} is the initial production activity in Nylon targets for each one of the positron emitters produced. The energies at which each production yield is measured is different for each stack of targets, since different thickness were used. Therefore, an interpolation of the production cross sections was performed when neeed.

As the production cross sections of ^{nat}O and ^{nat}N have been calculated subtracting the contribution of ^{nat}C in both cases, and the contribution of ^{nat}O in the ^{nat}N cross section, the uncertainty in each cross section depends on the uncertainty of the cross section subtracted.

The subtraction is sizeable in the case of ^{14}N(p,*)^{13}N, where it amounts to be 50%. In

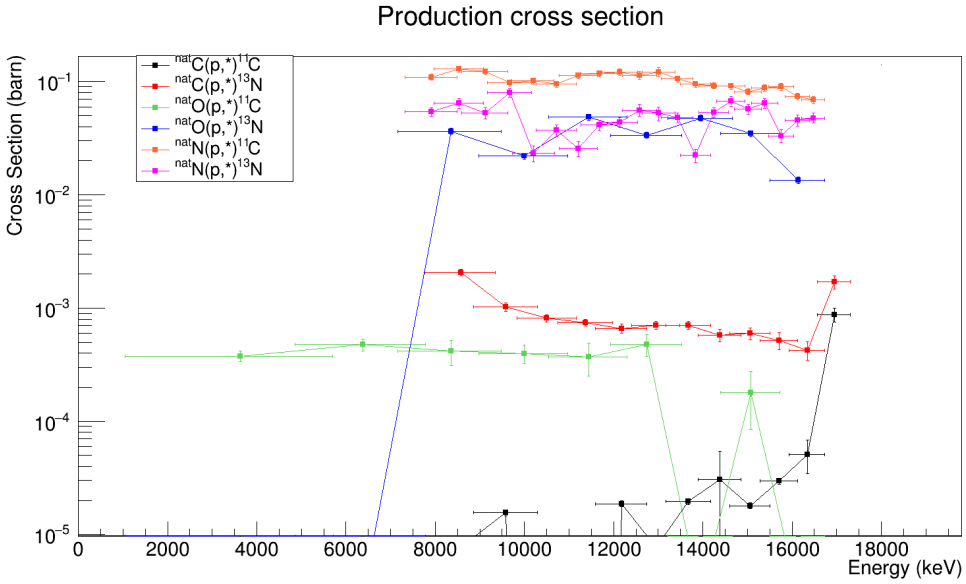

Figure 3.8: *Production cross section for nuclear reactions of interest.*

the reaction ^{14}N(p,*)^{11}C, the subtraction is less than 5%, whereas in ^{16}O(p,*) the subtraction ranges from 1% to 25%.

Tables 3.7, 3.8 and 3.9 contain the production cross sections of the positron emitters ^{11}C and ^{13}N, in ^{nat}C, ^{16}O and ^{14}N, respectively. The uncertainty in each value is calculated taking into account the uncertainties mentioned in section 3.2, as well as the error propagation in the subtraction of the measured cross section.

At this point it must be mentioned that the visual inspection of the PMMA films after the irradiation revealed that they had a plastic protection layer. This layer was found to add an amount of oxygen between 0 and 4% to the PMMA layer, depending if it is considered to be made of PE or EVA. This has been considered in the final cross section values, and also the fact that this layer contributes to a larger degradation in proton energy in each PMMA film.

The cross sections resulting from the mentioned measurement and analysis are shown in figure 3.8. A total of six cross sections have been measured between 4 and 17 MeV. The reactions with threshold have cross sections in the order of mb while the rest are between 0.02 and 0.1 barn. The comparison with previous measurements is presented in the following section.

Energy (MeV)	Cross section ^{11}C (mb)	Cross section ^{13}N (mb)
$17.0^{+0.4}_{-0.4}$	0.87 ± 0.12	1.71 ± 0.22
$16.3^{+0.4}_{-0.4}$	0.10 ± 0.03	0.33 ± 0.06
$15.7^{+0.4}_{-0.4}$	0.00362 ± 0.0022	0.51 ± 0.09
$15.1^{+0.4}_{-0.5}$	0.0179 ± 0.0011	0.60 ± 0.07
$14.4^{+0.5}_{-0.5}$	0.04 ± 0.03	0.56 ± 0.07
$13.7^{+0.5}_{-0.5}$	0.0196 ± 0.0018	0.70 ± 0.06
$13.0^{+0.5}_{-0.6}$	0.008 ± 0.004	0.70 ± 0.06
$12.2^{+0.6}_{-0.6}$	0.0186 ± 0.0011	0.66 ± 0.06
$11.4^{+0.6}_{-0.6}$	0 (*)	0.74 ± 0.05
$10.5^{+0.7}_{-0.7}$	0 (*)	0.81 ± 0.06
$9.6^{+0.7}_{-0.7}$	0.0155 ± 0.0009	1.02 ± 0.09
$8.6^{+0.8}_{-0.8}$	0.0079 ± 0.0004	2.07 ± 0.14

Table 3.7: Production cross section measurement in C_{nat}. (*) The results of these fit are too small and can not be trusted data, due to the low production yield of 11C in PE targets. Then the cross sections are compatible with zero.

Energy (MeV)	Cross section ^{11}C (barn)	Cross section ^{13}N (barn)
$16.1^{+0.6}_{-0.6}$	0 (*)	11.6 ± 0.8
$15.1^{+0.7}_{-0.7}$	0.15 ± 0.08	35.8 ± 2.1
$14.0^{+0.7}_{-0.7}$	0 (*)	48.8 ± 2.9
$12.7^{+0.8}_{-0.8}$	0.44 ± 0.10	34.4 ± 2.1
$11.4^{+0.9}_{-0.9}$	0.35 ± 0.11	49.7 ± 2.9
$10.0^{+1.0}_{-1.0}$	0.38 ± 0.07	23.3 ± 1.4
$8.4^{+1.1}_{-1.2}$	0.44 ± 0.11	41.2 ± 2.5
$6.4^{+1.4}_{-1.5}$	0.45 ± 0.05	4.9 ± 0.3
$3.6^{+2.1}_{-2.6}$	0.27 ± 0.03	0 (*)

Table 3.8: Production cross section measurement in ^{16}O. (*) The results of these fit are too small and can not be trusted data, due to the low production yield in comparison with the contribution of C producing ^{11}C and ^{13}N.

Energy (MeV)	Cross section ^{11}C (barn)	Cross section ^{13}N (barn)
$16.5^{+0.3}_{-0.3}$	68 ± 5	50 ± 5
$16.1^{+0.3}_{-0.3}$	76 ± 5	52 ± 6
$15.8^{+0.3}_{-0.3}$	92 ± 6	43 ± 6
$15.4^{+0.3}_{-0.3}$	89 ± 6	77 ± 8
$15.0^{+0.3}_{-0.3}$	83 ± 5	72 ± 7
$14.6^{+0.3}_{-0.3}$	92 ± 6	82 ± 8
$14.2^{+0.3}_{-0.3}$	92 ± 6	76 ± 8
$13.8^{+0.3}_{-0.4}$	95 ± 6	53 ± 7
$13.4^{+0.4}_{-0.4}$	106 ± 6	81 ± 8
$13.0^{+0.4}_{-0.4}$	116 ± 10	35 ± 5
$12.6^{+0.4}_{-0.4}$	109 ± 9	46 ± 5
$12.1^{+0.4}_{-0.4}$	118 ± 8	46 ± 5

$11.7^{+0.4}_{-0.4}$	116 ± 7	42 ± 5
$11.2^{+0.4}_{-0.4}$	112 ± 7	19 ± 3
$10.7^{+0.4}_{-0.5}$	94 ± 6	35 ± 4
$10.2^{+0.5}_{-0.5}$	101 ± 6	26 ± 4
$9.7^{+0.5}_{-0.5}$	97 ± 6	73 ± 7
$9.1^{+0.5}_{-0.5}$	123 ± 7	42 ± 5
$8.5^{+0.6}_{-0.6}$	130 ± 8	74 ± 7
$7.9^{+0.6}_{-0.6}$	109 ± 7	74 ± 7

Table 3.9: Production cross section measurement in ^{14}N.

3.4 Comparison to previous data

A comparison with the cross section data available in EXFOR database has been performed. In order to compare the production cross sections in ^{nat}C, the available cross sections for ^{12}C and ^{13}C are weighted by their relative abundance in natural carbon, as we can not distinguish between the contributions from these two isotopes. Figures 3.9-3.14 show the available data in EXFOR for the nuclear reactions of interest, as well as the production cross sections obtained in this study. The red arrow indicates the energy threshold for each reaction channel.

In the case of the reaction^{nat} C(p,*)^{11}C, the cross section measurements show that at low energies the production yields of ^{11}C is negligible, because of the threshold energy of 15 MeV. The fitting curves in this case are equally good fixing the initial activity of ^{11}C to zero, for energies lower than 16 MeV. Therefore, these experimental values can should be understood as an upper limit below the threshold of the production cross section.

The production cross section of ^{13}N in ^{nat}C is dominated by ^{13}C, with no data available for ^{12}C. Our cross section values follow the same behaviour than the data provided by M. L. Firouzbakht for ^{13}C. It can be observed that the results of this study are in good

agreement with the previous measurements done at CNA by J. Saiz, although the increase of cross section in the highest energy is surprising.

Regarding the cross sections in oxygen via the reaction channel ^{16}O(p,*)^{11}C, there is only one data point in the range of interest. The cross section in this work is in the order of 10^{-4} barns, with a sizeable uncertainty due to the subtraction of the carbon contribution in PMMA targets. Our result is in agreement with the value from Akagi.

The reaction channel ^{16}O(p,*)^{13}N has been extensively measured in a wide range of energy. There is ever an IAEA evaluated cross section (Takacs, 2003). Our cross section is in relatively good agreement with the data available, being on average 19% higher than the values of Takacs.

There is also a wide set of data available in the literature for the reaction channel ^{14}N(p,*)^{11}C. Again, there is an IAEA evaluated cross section by Tacaks (2003). Our data are in agreement, slightly higher, with previous data; although it is obvious that the measurement with a degraded beam from a cyclotron does not provide the same energy resolution as the linacs used in previous measurements.

Last, in the reaction ^{14}N(p,*)^{13}N, there are not an agreement between the data available in EXFOR (differences about 50%). The results of this study show that the production cross section at low energies are in a factor 5 above the data provides by Z. Kovacs, whereas cross section measurement of this work are in agreement with the previous measurements done at CNA by J. Saiz.

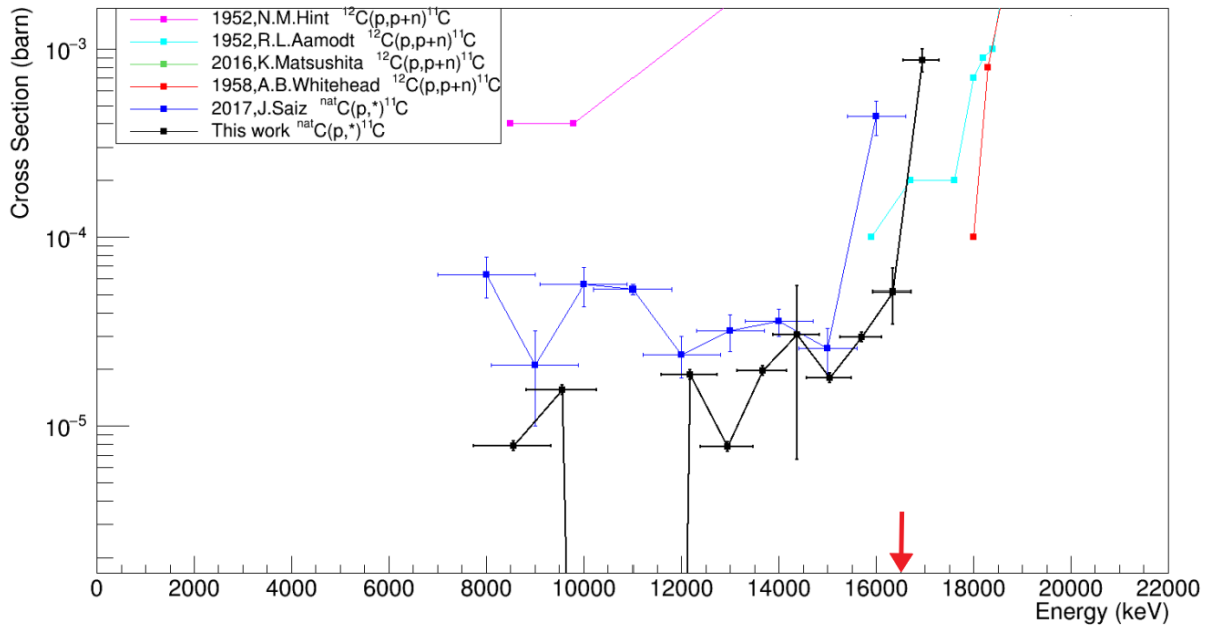

Figure 3.9: *Production cross section of positron emitter ^{11}C measured in ^{nat}C and the experimental data available in EXFOR.*

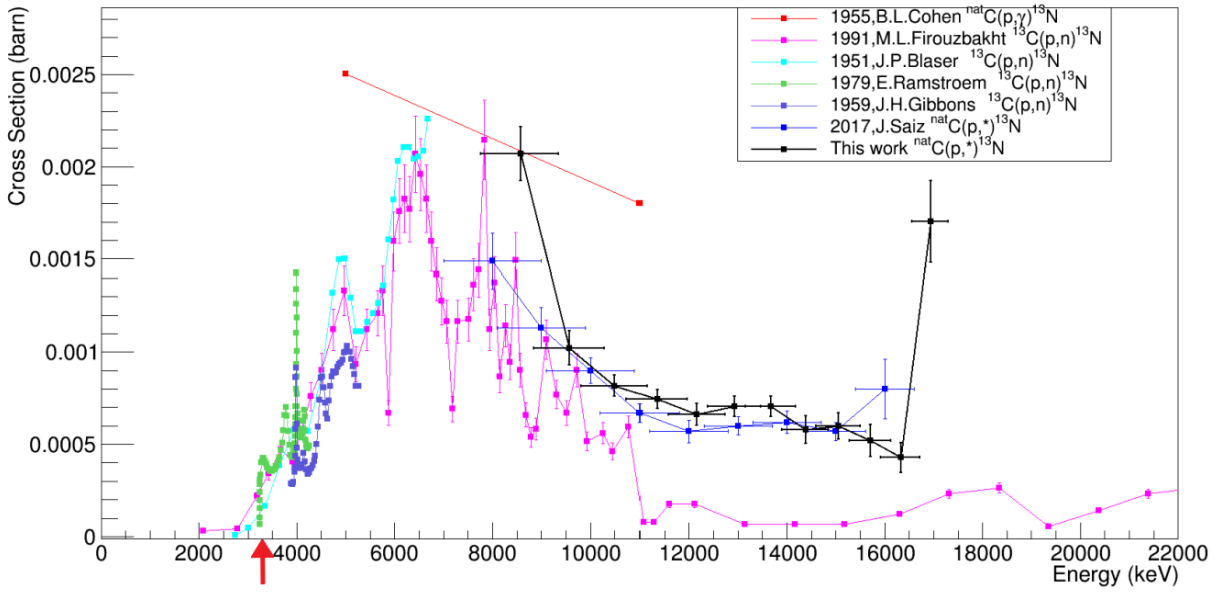

Figure 3.10: *Production cross section of positron emitter ^{13}N measured in ^{nat}C and the experimental data available in EXFOR.*

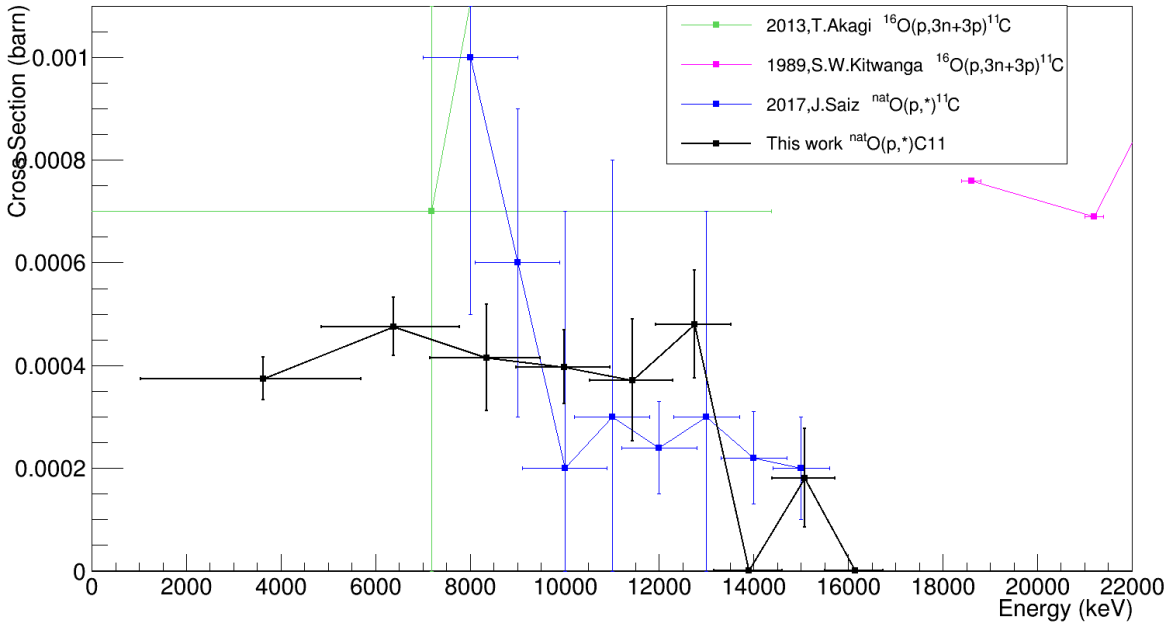

Figure 3.11: *Production cross section of positron emitter ^{11}C measured in ^{nat}O and the experimental data available in EXFOR. The threshold is out of the energy range.*

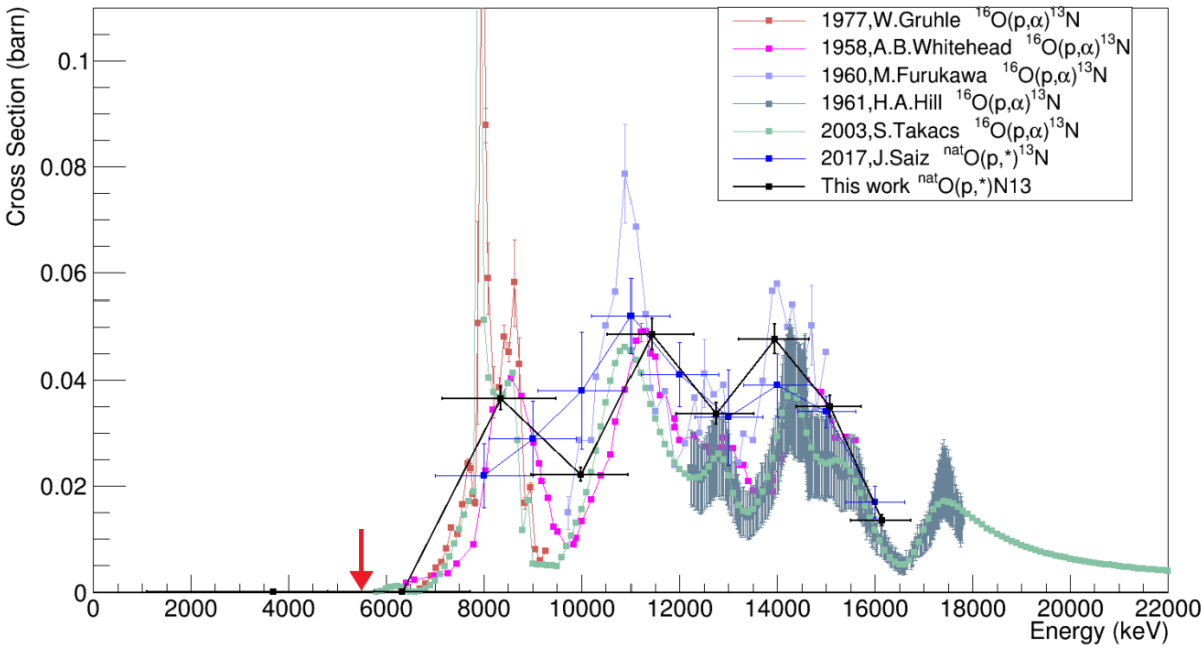

Figure 3.12: *Production cross section of positron emitter ^{13}N measured in ^{nat}O and the experimental data available in EXFOR.*

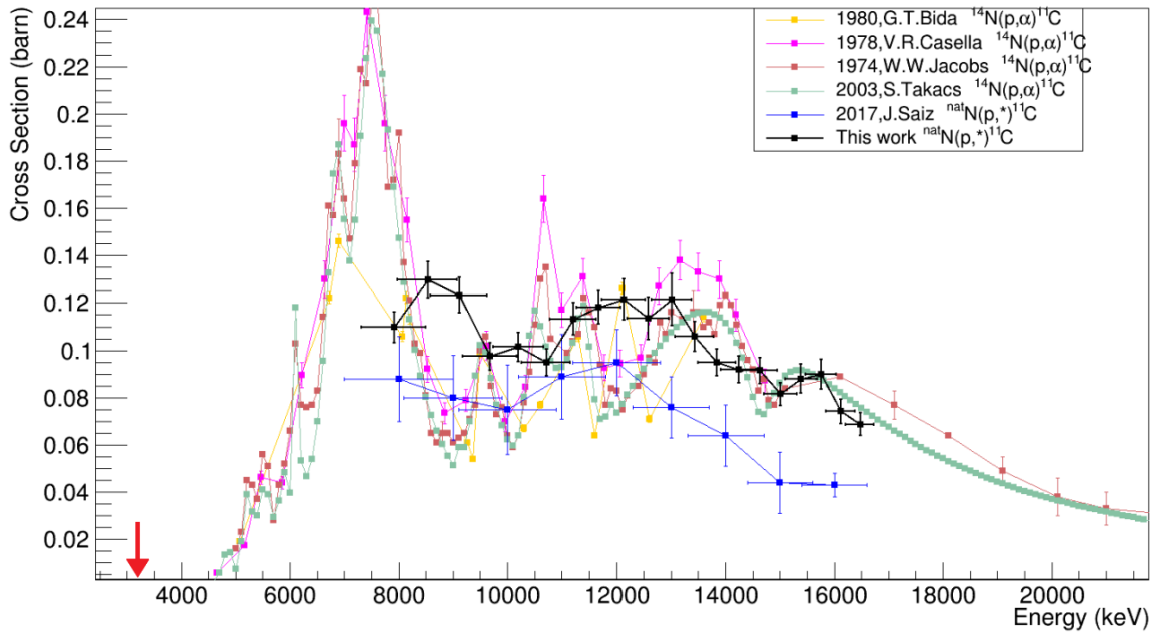

Figure 3.13: *Production cross section of positron emitter ^{11}C measured in ^{nat}N and the experimental data available in EXFOR.*

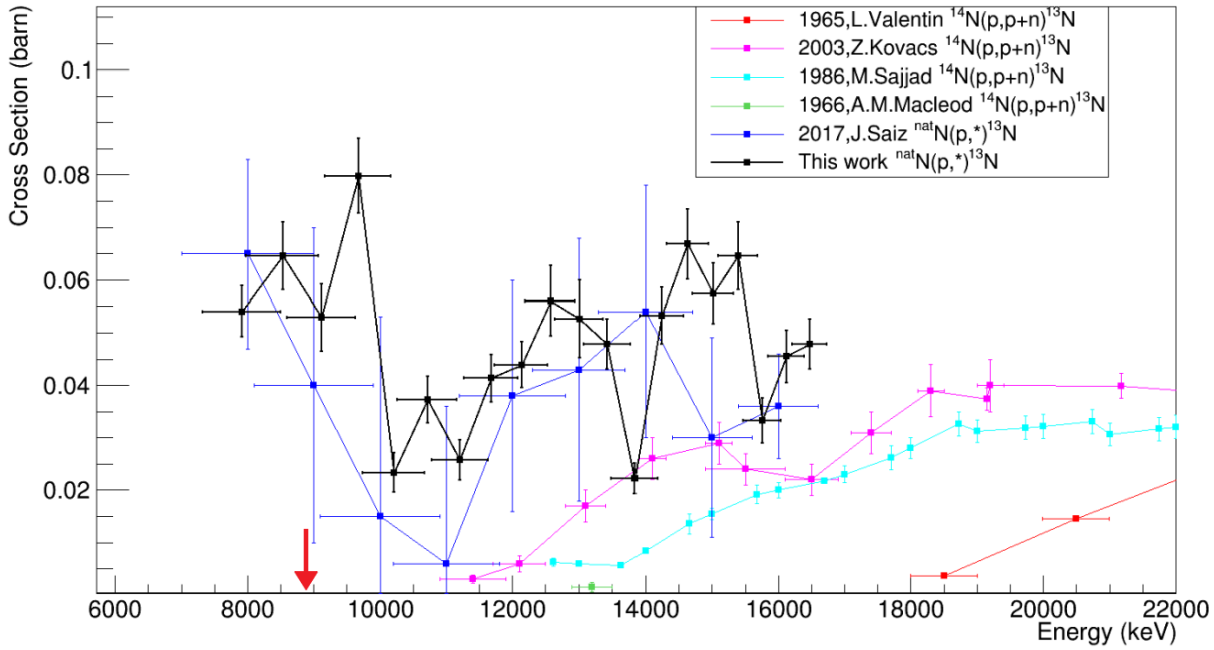

Figure 3.14: *Production cross section of positron emitter ^{13}N measured in ^{nat}N and the experimental data available in EXFOR.*

4. Conclusion and outlook

In this work the production cross sections of β^+ emitters for different reaction channels of interest in range verification have been measured. In order to do this, a stack of thin layers have been used to degrade the 18 MeV proton beam from the CNA cyclotron, permitting the measurement of the production cross sections of interest in each layer at a determined energy. In this way, the production cross sections have been measured in a energy range from 4 to 17 MeV.

A series of improvements in the experimental set up analysis tools with respect to a previous attempt have been developed. Regarding the experimental set up, a new sample holder for the irradiation have been designed and manufactured at CNA, in order to irradiate all the targets without having to access the bunker. In addition, a matrix of polyethylene (acting as conversor for the positrons) in which the films and the calibration source are placed during the PET acquisition has been designed and manufactured in the workshop of the Physics Faculty. Using this PE matrix and a known activity ^{22}Na source, an accurate spatial calibration in efficiency of the PET scanner has been performed.

In relation with the analysis of the experimental data, a correction by decay during the irradiation time has been introduced, allowing the comparison between the first PE layers in each stack of targets and the validation of the current beam measurement within 2%.

In order to reduce the possible systematic uncertainty in the measurement of the production cross section, a series of verification tests have been done, such as the measurement of the targets' thickness and the experimental determination of the ^{22}Na calibration source activity.

The result of the experiment is a set of six cross sections (^{nat}C(p,*)^{11}C, ^{nat}C(p,*)^{13}N, ^{nat}O(p,*)^{11}C, ^{nat}O(p,*)^{13}N, ^{nat}N(p,*)^{11}C, ^{nat}N(p,*)^{13}N) in the energy range between 4 and 17 MeV with an accuracy that ranges between a minimum systematic uncertainty of 6% from the measurement, and an additional contribution to the uncertainty from the fits of the activity curves that ranges from 1% up to 50% (see tables 3.7, 3.8 and 3.9 for details). In comparison with the available data in EXFOR database, our measurements of the production cross sections are in agreement within uncertainties with the different

authors when there is good quality of data, such as in the reaction channels $^{16}O(p,*)^{13}N$ and $^{14}N(p,*)^{11}C$. In addition, in certain energy range where there was not any available data, the production cross sections have been measured for the first time.

In summary, the experimental techniques, improvements and set up have been developed in order to measure successfully the production cross sections of interest below 18 MeV and this will allow in a near future measurements at clinical energies (up to 250 MeV) at other international facilities.

Bibliography

[1] W.D. Newhauser and R. Zhang, "The physics of proton therapy", *Phys. Med. Biol. 60*, p. R155-R209, 2015.

[2] R. R. Wilson, "Radiological use of fast protons", *Radiology, vol. 47, no. 5*, p. 487-491, 1946.

[3] J. H. Lawrence et al., "Pituitary irradiation with high-energy proton beams a preliminary report", *American Association for Cancer Research*, vol. 18, no. 2, p. 121-134, 1958.

[4] R. Kjellberg et al., "Stereotaxic instrument for use with the Bragg peak of a proton beam", *Confinia Neurol.*, vol. 22, 1962a.

[5] R. Kjellberg et al., "The Bragg peak of a proton beam in intracranial therapy of tumors", *Transactions of the American Neurological Association (U.S.)*, vol. 87, 1962b.

[6] E. Gragoudas et al., "Proton beam irradiation of uveal melanomas: Results of 5.5-year study", *Archives of Ophthalmology*, vol. 100, no. 6, p. 928-934, 1982.

[7] A. M. Koehler et al., "Flattening of proton dose distributions for large-field radiotherapy", *Medical Physics*, vol. 4, no. 4, p. 297-301, 1977.

[8] https://www.ptcog.ch. "Particle Therapy Co-Operative group".

[9] W.P. Levin et al., "Proton beam therapy", *British Journal of Cancer, 93*, p. 849-854, 2005 .

[10] H. Bethe, "Zur theorie des durchgangs schneller korpuskularstrahlen durch materie", *Ann. Phys.*, no. 5, p. 324-400, 1930.

[11] F. Bloch, "Zur bremsung rasch bewegter teilchen beim durchgang durch materie", *Ann. Phys.*, no. 16, pp. 285-320, 1933.

[12] H. Paganetti, "Proton beam therapy", *Proton Beam Therapy*, IOP Publishing, p. 1-5, 2017.

[13] H. Paganetti, "Range uncertainties in proton therapy and the role of Monte Carlo simulations", *Phys. Med. Biol. 57 R99*. 2012.

[14] P. Dendooven et al., "Short-lived positron emitters in beam-on pet imaging during protontherapy", *Phy. Med. Biol. 60*, p.8923-8947.

[15] X. Zhu et al, "Proton Therapy Verification with PET Imaging", *Theranostics*, 3(10):731-740, 2013.

[16] F. Hueso-González et al., "Compton camera and prompt gamma ray timing: two methods for in vivo range assessment in protontherapy", *Frontiers in Oncology* 6: 80, 2016.

[17] https://www-nds.iaea.org/exfor/exfor.htm Website of experimental nuclear reaction data.

[18] S. España et al., "Reliability of proton-nuclear interaction cross section data to predict proton-induced PET images in proton therapy", *Phy. Med. Biol. 56*, p. 2687-2698, 2011.

[19] K. Parodi et al., "Experimental study on the feasibility of in-beam PET for accurate monitoring of proton therapy", *IEEE Transactions on Nuclear Science, vol. 52, no. 3, 2005*

[20] J. Saiz, "Measurement of β^+ emitters production cross sections of interest for range verification in proton therapy", Master's thesis, U. de Sevilla, 2017.

[21] http://cna.us.es/ Website of Centro Nacional de Aceleradores.

[22] T. Akagi et al., "Experimental study for the production cross sections of positron emitters induced from ^{12}C and ^{16}O nuclei by low-energy protons beams", *Radiation Measurements 59*, p. 262-269, 2013.

[23] J. F. Ziegler, "The stopping and range of ions in matter." http://www.srim.org/.

[24] K. Parodi et al., "PET/CT imaging for treatment verification after proton therapy: A study with plastic phantoms and metallic implants", *Med. Phys.* 34(2): 419-435, 2007.